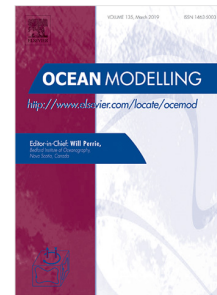# Journal Pre-proof

Assessment of a regional physical-biogeochemical stochastic ocean model. Part 2: Empirical consistency

Vassilios D. Vervatis, Pierre De Mey-Frémaux, Nadia Ayoub,
John Karagiorgos, Stefano Ciavatta, Robert J.W. Brewin,
Sarantis Sofianos

Please cite this article as: V.D. Vervatis, P. De Mey-Frémaux, N. Ayoub et al., Assessment of a regional physical-biogeochemical stochastic ocean model. Part 2: Empirical consistency. *Ocean Modelling* (2021), doi: https://doi.org/10.1016/j.ocemod.2021.101770.

This is a PDF file of an article that has undergone enhancements after acceptance, such as the addition of a cover page and metadata, and formatting for readability, but it is not yet the definitive version of record. This version will undergo additional copyediting, typesetting and review before it is published in its final form, but we are providing this version to give early visibility of the article. Please note that, during the production process, errors may be discovered which could affect the content, and all legal disclaimers that apply to the journal pertain.

1 **Assessment of a regional physical-biogeochemical stochastic ocean model. Part 2:**
2 **empirical consistency**

3 Vassilios D. Vervatis (1), Pierre De Mey-Frémaux (2), Nadia Ayoub (2), John Karagiorgos (1),
4 Stefano Ciavatta (3, 4), Robert J. W. Brewin (3, 5), and Sarantis Sofianos (1)

5 (1) University of Athens, Department of Physics, Athens, Greece. (2) LEGOS/CNRS,
6 Toulouse, France. (3) Plymouth Marine Laboratory, Plymouth, UK. (4) National Centre for
7 Earth Observation, Plymouth, UK. (5) University of Exeter, College of Life and Environmental
8 Sciences, Penryn, Cornwall, UK.

9 *Correspondence to*: Vassilios D. Vervatis (vervatis@oc.phys.uoa.gr)

10 **Abstract.** In this Part 2 article of a two-part series, observations based on satellite missions
11 were used to evaluate the empirical consistency of model ensembles generated via stochastic
12 modelling of ocean physics and biogeochemistry. A high-resolution Bay of Biscay
13 configuration was used as a case study to explore the model error subspace in both the open
14 and coastal ocean. In Part 1 of this work, three experiments were carried out to generate model
15 ensembles by perturbing only physics, only biogeochemistry, and both of them simultaneously.
16 In Part 2 of this work, empirical consistency was checked, first by means of rank histograms
17 projecting the data onto the model ensemble classes, and second, by pattern-selective
18 consistency criteria in the space of "array modes" (eigenvectors of the representer matrix).
19 Rank histograms showed large dependency on geographical region and on season for sea
20 surface temperature (SST), sea-level anomaly (SLA), and phytoplankton functional types
21 (PFT), shifting from consistent model-data configurations to large biases because of model
22 ensemble underspread. Consistency for SST array modes was found to be verified at large,
23 small and coastal scales soon after the ensemble spin-up. Array modes for the along-track sea-
24 level showed useful consistent information at large scales and at the mesoscale; for the gridded
25 SLA was verified only at large scale. Array modes showed that biogeochemical model
26 uncertainties generated by stochastic physics, were effectively detected by PFT measurements
27 at large scales, as well as at mesoscale and small-scale. By contrast, perturbing only
28 biogeochemistry, with an identical physical forcing across the ensemble, limits the potential of
29 PFT measurements at detecting and possibly correcting small-scale biogeochemical model
30 errors. When an ensemble was found to be inconsistent with observations along a particular
31 direction (here, an array mode), a plausible reason is that other error processes must have been
32 active in the model, in addition to the ones at work across the ensemble.

33 **Keywords:** stochastic modelling, ensembles, phytoplankton functional types, prior error
34 covariances, array modes, Bay of Biscay

35 **1   Introduction**

36 In the coastal parts of regional ocean models, many factors can complicate the assimilation of
37 data. One of them is the characterization and specification of model errors, which are critical
38 in any assimilation scheme, but extremely challenging in the coastal zone. Ocean model errors
39 strongly depend on spatiotemporal scales, though any attempt at separation is confounded by
40 strong nonlinearity in the dynamics that can couple variability at different frequencies and
41 wavenumbers (*Auclair et al.*, 2003). Another factor complicating data assimilation is the
42 specification of observational errors, which are made up of measurement (usually small) and
43 representativity errors (usually large or unknown), and cross-correlations between observations
44 (usually unknown) (*Oke and Sakov*, 2008).

45 Most studies point at the benefit of advanced assimilation methods with built-in error
46 propagation (*Kourafalou et al.*, 2015a; 2015b), such as the Ensemble Kalman Filter (EnKF;

47 *Evensen*, 2003) and variants. As a first step, one must characterize the forecast uncertainties
48 under various error regimes (situations where the model is in error), either in response to time-
49 varying forcing errors (e.g. uncertainties in boundary conditions; *Ghantous et al.*, 2020) or due
50 to internal sources (e.g. model parameterizations; *Brankart et al.*, 2015), and include realistic
51 error dynamics through stochastic modelling. For instance, depending on the wind regime, or
52 seasonal baroclinic instabilities of the slope current, shelf errors can be different in terms of
53 spatiotemporal scales (*Auclair et al.*, 2003). Biogeochemical model errors can also be different
54 stemming from unresolved scales and biodiversity (*Garnier et al.*, 2015). It should be noted
55 that stochastic modelling, in itself, may not yield realistic error dynamics, for example, it could
56 inflate the ensemble (*Anderson*, 2009).

57 In the companion article Part 1 (*Vervatis et al.*, 2021), we configured a high-resolution (1/36°)
58 stochastic ocean model for the Bay of Biscay performing physical-biogeochemical ensemble
59 simulations. We carried out quantitative assessment of model-data misfits and qualitative
60 evaluation of multivariate incremental analysis. We found that the skill of the perturbation
61 method to generate model errors was improved (in general) for physics compared with
62 biogeochemical perturbations in source and sink terms (i.e. larger ensemble spread when
63 physics is perturbed) and that the data assimilation performance to correct those model errors,
64 was largely dependent on the chosen multivariate analysis. On the other hand, the
65 biogeochemical model spread was found under-dispersive, leading to disjoint supports[1] of the
66 model and data probability density functions (pdf), and performance was mainly defined by
67 the assimilation of ocean colour data, possibly because of weak cross-covariances between
68 ocean physics and biogeochemistry.

69 In light of these findings, in this companion article Part 2, we present two methods to evaluate
70 the consistency with respect to observations (hereafter empirical consistency) of a stochastic
71 coupled ocean model, which comes in the form of an ensemble of multivariate ocean states.
72 We focus on observational products including physics and biogeochemistry, derived from
73 satellite missions monitoring upper-ocean properties, such as the sea surface temperature
74 (SST), the sea-level anomaly (SLA) and an ocean colour product of phytoplankton functional
75 types (PFT; *Brewin et al.*, 2010; 2015; 2017). Several biogeochemical studies have focused on
76 improving the model's predictive skill using remote sensing and in-situ observations,
77 incorporating data assimilation and probabilistic attribution (*Candille et al.*, 2015; *Song et al.*,
78 2016; *Gharamti et al.*, 2017; *Mattern et al.*, 2018; *Ford*, 2019). Here, we focus our analysis on
79 the use of ocean colour PFT observations following recent advances in data assimilation to
80 improve marine ecosystem simulations (*Ciavatta et al.*, 2018; 2019).

81 In a probabilistic framework, the support of the joint pdf of observed and forecast values
82 should be non-null in order to enable data assimilation. In other words, the prior model state
83 and the data must be compatible with each other given their respective uncertainties in order
84 for assimilation to be meaningful. Therefore, one important question we address in this study
85 is the following: is the distribution of the forecast errors estimated from the ensemble (the prior
86 distribution) compatible with the distribution of the data to be assimilated? Another important
87 question is about how ensembles (e.g. the state of a stochastic model) can be validated – in
88 effect, ensembles are not used solely for assimilation – other uses include: array design,
89 probabilistic forecasting, a learning base for artificial intelligence applications, etc.

90 As a first step, we assess the empirical consistency of ensembles by means of rank histograms
91 (also referred to as Talagrand diagrams; *Candille and Talagrand*, 2005) projecting the data

---

[1] The support of a probability density function *(pdf)* is the smallest closed set outside of which the *pdf* vanishes.
For a *pdf* defined in ℝ, the *pdf* envelope (i.e. here the ensemble envelope) is the range between the minimum and
maximum values of the support.

92 onto the model ensemble classes. Rank histograms are useful for diagnosing reliability and
93 inferring systematic biases in an ensemble prediction system (*Hamill,* 2001). As a second step,
94 we apply a *consistency diagnostic on innovations* inspired by the similarly-named diagnostic
95 developed in *Andersson* (2003) and *Desroziers et al.* (2005) in the framework of the assessment
96 of the well-posedness of data assimilation schemes. Our implementation is however specific
97 in two ways: (1) we use that metric here outside of a data assimilation scheme, to check how
98 consistent our ensembles are with respect to innovations; (2) we project the innovation
99 consistency diagnostic on *Array Modes*, with the objective of permitting pattern-dependent
100 consistency analysis. Our definition of array modes follows previous publications (*Le Hénaff*
101 *et al.,* 2009; *Lamouroux et al.*, 2016; and *Charria et al.*, 2016). This is detailed below.

102 This study is organized as follows. Section 2 describes the stochastic approach to generate
103 model ensembles, following the companion article Part 1. The specifications of the
104 observational networks are presented in Section 3, including the description of the ocean colour
105 PFT. A summary of the consistency analysis framework based on rank histograms and array
106 modes is given in Section 4, which presents also a new criterion in "array space". The results
107 and conclusions are discussed in Sections 5 and 6.

2   Stochastic modelling

109 We used the NEMO platform (Nucleus for European Modelling of the Ocean;
110 http://www.nemo-ocean.eu/; *Madec,* 2012) and its biogeochemical component PISCESv2
111 (Pelagic Interactions Scheme for Carbon and Ecosystem Studies volume 2; *Aumont et al.,*
112 2015). The ocean model domain encompasses the Bay of Biscay and the western part of the
113 English Channel (*Quattrocchi et al.,* 2014; *Vervatis et al.,* 2016). The physical model is
114 coupled online (one-way with high coupling frequency for the conservation of tracers) with a
115 biogeochemical model at 1/36° horizontal resolution.

116 Three seasonal-range ensembles were carried out using stochastic modelling of ocean physics
117 and biogeochemistry as part of the project SCRUM (Stochastic Coastal/Regional Uncertainty
118 Modelling; cf. companion article Part 1 by *Vervatis et al*. 2021). Perturbations were modelled
119 using first-order auto-regressive processes - AR(1) - in the context of stochastic perturbed
120 parameterized tendencies (SPPT; *Buizza et al.,* 1999) and stochastic perturbed parameters
121 (SPP; *Ollinaho et al.*, 2017). The AR(1) processes were different for each perturbed tendency
122 or parameter, and varied under the assumption of spatiotemporal correlated scales. A
123 deterministic free run was performed from July 2011 to November 2011, to serve as a five-
124 month model spin-up starting from ocean analyses for the whole state vector, and then extended
125 from December 2011 to June 2012, to serve as reference for the main physical and
126 biogeochemical processes in the region and deduce the statistical properties for the AR(1)
127 stochastic parameterizations. The ensemble simulations were initialized from the five-month
128 spin-up and carried out from December 2011 to June 2012. The 40-member ensembles were
129 used to estimate the forecast error covariance matrix perturbing different sources of model
130 errors.

131 In Table 1, we summarize the stochastic protocol for the three ensembles, hereafter referring
132 to them as: EnsP - perturbing physics under the assumption of atmospheric forcing
133 uncertainties and model uncertainties in physical parameterizations; EnsB - perturbing
134 biogeochemistry under the assumption of model uncertainties in biogeochemical sources and
135 sinks; and EnsPB - perturbing both physics and biogeochemistry. The biogeochemical model
136 parameters were not perturbed. The initial conditions were also not perturbed. The EnsPB is
137 statistically identical to EnsP for model errors in ocean physics, because there is no feedback
138 to the physics from the biogeochemical model. By contrast, EnsPB is statistically different to
139 EnsB and EnsP because uncertainties in the physical forcing are found to have a large impact

3

140 on biogeochemical model properties. Also, for the EnsB the physics and hence the circulation
141 are the same for all members. For details of the physical-biogeochemical model and for model
142 data ensemble-based misfits, the reader is referred to the companion article Part 1.

143 The model uncertainties in physical and biogeochemical properties in the upper ocean are
144 described in Part 1. Here we illustrate the typical patterns that we obtained for the spread in
145 SST, sea surface height (SSH) and chlorophyll abundance at specific dates that will also serve
146 as a reference for the analyses in Section 5. Figure 1a shows, the Bay of Biscay SST from the
147 deterministic simulation on May 31, 2012. Fig. 1b shows the EnsP model ensemble spread for
148 SST on the same date. Figs. 1a-b show that the ocean model solution and its associated error
149 structures for SST are statistically consistent. In more detail, error regimes are linked to
150 physical processes controlling SST, for example, the extension of the Ushant thermal tidal front
151 west of Brittany in the English Channel. At that time of the year, the stratification is strong and
152 the freshwater front (due to the Loire and Gironde rivers runoff in the Armorican shelf) leads
153 to a large spread locally exceeding $0.8\,°C$. Figs. 1c-d give an insight of the model circulation
154 patterns on February 25, 2012, depicted by SSH and their error structures. After a two-month
155 spin-up period, the maxima of SSH model spread are collocated with mesoscale eddies
156 observed in the abyssal plain, and with (most likely) inertial barotropic waves observed over
157 the shelves. The perturbation mechanism works throughout the whole period. Therefore, the
158 SSH spread continues to grow in the abyssal plain due to mesoscale decorrelation of eddies
159 across members (not shown).

160 Figure 2a shows the total chlorophyll abundance of the deterministic simulation at the onset of
161 the spring bloom on March 28, 2012. In Figs. 2b-d, and for the same date, we show model
162 uncertainties in total chlorophyll for the three ensembles EnsP, EnsB and EnsPB. We
163 emphasize two important findings: first, the model errors in physics have a larger impact on
164 chlorophyll model uncertainties compared with those generated by perturbing the
165 biogeochemical model source and sink terms; second, the chlorophyll spread is increased when
166 model physics and biogeochemistry are perturbed simultaneously. However, there are also
167 exceptions of decreasing spread (e.g. occurring locally in the presence of coherent eddies).
168 Interestingly, an uneven ensemble spread is also observed between nanophytoplankton and
169 diatoms chlorophyll (Figs. 2e-f). Model errors for each phytoplankton type follow the different
170 patterns of their chlorophyll concentrations, with large uncertainties observed in the abyssal
171 plain for nanophytoplankton, and on the shelves and the English Channel for diatoms.

3 Observational networks

173 In this study, although we examine the same broad categories of observations as in the
174 companion article Part 1, we have included more satellite products observing the upper-ocean
175 physical and biogeochemical properties. Therefore, for the sake of clarity, we have included a
176 full description of observations. We consider global and regional satellite products monitoring
177 the Bay of Biscay, using high-level L3 and L4 merged data from multi-missions for both real-
178 time and delayed modes. All datasets are provided at daily frequency. This level of data quality
179 is often required in ocean forecasting systems for model validation and data assimilation. Table
180 2 summarizes the datasets used for the empirical consistency analysis and their specifications
181 are given briefly in the paragraphs below.

3.1 SST gridded observations

183 We chose two high-resolution SST L4 products, namely the OSTIA SST global dataset and the
184 regional Atlantic European north west shelf (NWS) SST. High-resolution SST data are
185 necessary when it comes to validate eddy-resolving model ensembles. Both networks are able

186   to resolve mesoscale eddy variability and frontal activity near the coasts, ranging from a few
187   kilometres over the shelves to scales of tens of kilometres in the open ocean.

188   The OSTIA SST is provided on a global regular grid at 0.05^o resolution (*Donlon et al.*, 2012)
189   and is by construction free of diurnal variability with a reference depth of 10 meters, referred
190   also as foundation SST. The reconstructed fields consist of L4 daily gap-free maps. The product
191   includes multi-sensor measurements from both infra-red and microwave instruments, as well
192   as in-situ observations retrieved from ships of opportunity, drifters and buoys. The data were
193   reprocessed using optimal interpolation and include a bias correction.

194   The NWS SST product is delivered at 0.04^o high horizontal resolution and consists of L4 daily
195   gap-free regional maps. Calculations are derived from infra-red measurements using only
196   night-time observations, and thus the NWS SST data are not affected by diurnal warming.

3.2   SLA gridded and along-track observations

198   We selected two products based on different levels of processing. The L3 along-track sea-level
199   product is based on several altimetric missions, specifically on Envisat and Cryosat-2 satellites.
200   The L4 gridded product was generated by reprocessing multi-mission altimetry data over many
201   years.

202   For the along-track data, we used the filtered sub-sampled L3 product with 14 km distance
203   between successive points along the altimetry track. The effective resolution of the data is
204   coarser than the aforementioned distance (*Pujol et al.*, 2016). The inverse barometer response
205   and the tides have been removed from the data (and the model, cf. companion article Part 1).

206   The L4 product is a merge of multi-mission satellites spanning the last two decades. The result
207   is a homogenous and consistent gridded dataset at a resolution of 0.25^o. The scales resolved
208   by the L4 gridded product depend on various factors, such as the quality of the L3 input data,
209   the sampling of the altimeter constellation and the optimal interpolation, which limits the
210   capability of the data to resolve part of the mesoscale (*Chelton et al.*, 2011).

3.3   Phytoplankton functional types ocean colour observations

212   We selected the regionally-tuned PFT satellite model of *Brewin et al.* (2017). The approach is
213   a modification of the three-component model of *Brewin et al.* (2010; 2015) and produces
214   estimates of the chlorophyll concentration of four phytoplankton groups (picophytoplankton,
215   nanophytoplankton, diatoms and dinoflagellates), as a function of the total chlorophyll
216   concentration, accounting for the influence of SST on model parameters. The model was tuned
217   and validated using a large dataset collected in the North Atlantic, inclusive of our region of
218   interest. The approach was run using ocean colour data from the ESA ocean colour climate
219   change initiative (OC-CCI) and OSTIA SST data. Products were produced on a regular grid at
220   0.05^o resolution. The data has been used successfully in PFT data assimilation exercises in the
221   North Atlantic (*Ciavatta et al.*, 2018; *Skakala et al.*, 2018). The products were developed in
222   the framework of the Copernicus Marine Environment Monitoring Service (CMEMS)
223   "Towards Operational Size-class Chlorophyll Assimilation (TOSCA)" Service Evolution
224   project.

225   The mismatch between biogeochemical model variables and ocean colour products has been
226   highlighted recently in an IOCCG Report No. 19 (*IOCCG*, 2020). The biogeochemical model
227   PISCES distinguishes two classes of chlorophyll, namely the nanophytoplankton and diatoms.
228   These two chlorophyll classes were given this name, as the traits of these modelled functional
229   types are closest to these two abundant groups in the natural world. However, these two classes
230   are designed to be representative of the entire phytoplankton community, and therefore are far
231   broader than the names imply. Each of the two model compartments encompasses a large range

5

232 of cell sizes, approximately representing smaller and larger phytoplankton types in the
233 biogeochemical model. In order to compare the observations with the model ensembles, we
234 decided to follow a size class-based categorization (*Sieburth et al.*, 1978) and group the four
235 ocean colour PFT into two phytoplankton types and keep the total chlorophyll concentration
236 in the data unchanged (i.e. the sum of all four types). For this, we combined the concentrations
237 of ocean colour pico- and nano- PFT into one small class comparable with the PISCES
238 nanophytoplankton, and the diatoms and dinoflagellates ocean colour PFT into one large class
239 comparable with the PISCES diatoms. This categorization took into consideration many
240 processes and biogeochemical cycles in the model, for example, not just the silicate cycle but
241 also the carbon and nitrogen cycles, and the size-selective feeding by microzooplankton and
242 mesozooplankton. However, it was unavoidable to combine one PFT with characteristic
243 silicate limitation with one without (i.e. diatoms and dinoflagellates; in supplementary material
244 we provide also an analysis without this combination). The choice to include all four PFT was
245 supported by the fact that their sum ensures the total biomass (chlorophyll) and therefore,
246 model and satellite total chlorophyll data can be compared like-for-like. In addition, the total
247 chlorophyll concentration (sum of the four PFT) in the model is of the same magnitude as the
248 total chlorophyll of other ocean colour products used for the validation of our ensembles, as
249 shown in the companion article Part 1 and in the supplementary material.

3.4 Observational errors

251 An estimate of the observational error is given by the measurement and representativity errors
252 (usually unknown) (*Desroziers et al.*, 2005; *Oke and Sakov*, 2008; *Janjić et al.*, 2018). The
253 measurement errors are usually small and refer to the instrument's sensor accuracy and data
254 processing. The representativity errors are usually large and can account for different model
255 and observation sampling schemes, or for the physical-biogeochemical signal that is contained
256 in the observations but is not represented in the model. Some of the data used here were
257 retrieved from archives and included a spatial distribution of their errors. While this
258 information is important for a dynamically heterogeneous system such as the Bay of Biscay,
259 we chose not to use it because it would be hard to interpret pattern-dependent consistency
260 results. Instead, we used a representative constant error for each observational network
261 provided by the CMEMS infrastructure and the data providers.

262 Assuming that errors are uncorrelated and that the innovation variance is therefore close to the
263 sum of model and data error variances, we considered an error standard deviation for SST equal
264 to $0.5\,^oC$, for SLA equal to $0.05\,m$, and for PFT equal to $0.3\,mg/m^3$ (Table 2). The satellite
265 chlorophyll *a* data are provided with a scaled (%) observational error in comparison to the
266 signal and therefore, the error has spatial distribution. We chose this constant PFT error over
267 an error that scales with the satellite chlorophyll *a* signal for the reason explained in the
268 paragraph above. The static PFT error is representative for the region, though moderately larger
269 for total chlorophyll and nanophytoplankton in the open ocean, and underestimated for diatoms
270 over the shelves, if compared with the PFT errors estimated by *Brewin et al.* (2017).

271 In the following Section 4, and for each of the consistency analysis methods, we discuss the
272 perturbation of observations to generate data distributions and the anamorphosis functions
273 applied to transform those distributions in the proper space (*Simon and Bertino*, 2009).

4 Consistency analysis framework

275 In this study, we implemented two empirical consistency analysis methods to evaluate model
276 ensembles with respect to observations. The first approach was based on rank histograms and
277 the second on array modes. The calculations were performed with a toolbox (nicknamed
278 "scrumcat": SCRUM consistency analysis toolbox) built upon the Sequoia Data Assimilation

6

279 Platform (SDAP; De Mey-Frémaux, 2020: https://sourceforge.net/projects/sequoia-dap/). The
280 implementation details are given below.

4.1 Rank histograms

282 The rank histogram (Talagrand diagram; *Candille and Talagrand*, 2005) is a verification metric
283 testing the empirical consistency between model samples and observations. An ensemble of m
284 members defines $m + 1$ ranks including the rank of one observation sorted within the model
285 ensemble. The steps to calculate rank histograms are (1) project ensemble samples in data space
286 using an observation operator, (2) sorting the ensemble samples by value, (3) ranking the
287 observed value within the sorted ensemble at each observation location, (4) tally over many
288 observations in space and time. We note that for the rank histograms the observations are not
289 perturbed and the model ensemble distributions are not checked for gaussianity.

290 The rank histogram is useful for determining the reliability of ensemble forecasts (*Hamill,*
291 *2001*) and is often used as a tool to infer systematic biases of an ensemble prediction system,
292 as well as differing spreads between model and data (e.g. small spread translates into most data
293 falling into the outer classes of the rank histogram). The rank histogram flatness is a measure
294 of the reliability of the ensemble prediction system and is estimated according to the definition
295 of statistical consistency by *Anderson* (1996) and *Candille and Talagrand* (2005):

$$\Delta = \sum_{i=1}^{m+1}\left(S_i - \frac{p}{m+1}\right)^2, \ \Delta_o = \frac{p*m}{m+1}, \ \delta = \frac{\Delta}{\Delta_o}\sim 1, \qquad (1)$$

297 where p is the number of observations, m the number of ensemble members, S_i the outcomes
298 in each rank (i.e. number of observations of rank i), Δ the deviation of the histogram from
299 flatness, Δ_o the expectation for a reliable system and δ the ratio measuring the reliability for a
300 scalar variable of the ensemble prediction system.

4.2 Ensemble consistency in array space

302 Rank histograms provide a way to check ensemble empirical consistency in a global,
303 distribution-like manner. In a complementary manner, we wish to complete the global analysis
304 with pattern-selective consistency analysis, using patterns which would be (A) hierarchized,
305 (B) representative of error covariances (as estimated from the ensemble) and (C) observable
306 by the data array. To that end, we chose to assess consistency in the space of *Array Modes*,
307 hereafter nicknamed "array space".

308 We use whenever possible the unified notations of data assimilation as in *Ide et al.* (1997). We
309 define *array modes* $\boldsymbol{\mu}$ as the eigenmodes of the *scaled representer matrix* $\boldsymbol{\chi}$ defined as:

$$\boldsymbol{\chi} \equiv \boldsymbol{R}^{-\frac{1}{2}}\boldsymbol{H}\boldsymbol{P}^f\boldsymbol{H}^T\boldsymbol{R}^{-\frac{1}{2}} = \boldsymbol{\mu}\boldsymbol{\sigma}\boldsymbol{\mu}^T \qquad (2)$$

311 where $\boldsymbol{P}^f$ is the *forecast (prior) error covariance matrix*, here approximated as an ensemble
312 covariance, $\boldsymbol{R}$ is the *observational error covariance matrix*, and $\boldsymbol{H}$ is the "classic" linear
313 *observation operator*. Because an observing array will not be concomitant, all operators are
314 four-dimensional in that they span time in addition to space.

315 These array modes have been discussed in several articles in the literature. First, *Le Hénaff et*
316 *al.* (2009) presented the theoretical background for the representer matrix spectra methodology,
317 aiming at assessing the performance of observational networks at detecting model errors. In
318 their study, prior model errors were generated via stochastic modelling of the wind forcing and
319 various altimetry and in-situ array deployment strategies were tested. Two other studies
320 followed, based on array modes, by *Lamouroux et al.* (2016) and *Charria et al.* (2016), where
321 authors designed optimal observation network experiments based on array modes, for the
322 future implementation of efficient integrated ocean observing systems monitoring the coastal

323 environment. Array modes are the eigenmodes of the representer matrix as approximated as an
324 ensemble covariance (e.g. from Section 2 ensembles). It follows that array modes meet the
325 pattern definition criteria (A-C) above.

326 The matrix χ in Eq. (2) expresses how the array "sees" the model uncertainties; the diagonal
327 matrix $\sigma = diag\{\sigma_k\}$ offers the same information as χ in array space, but in a diagonal form:
328 it is the *array mode spectrum*. Intuitively, the higher the eigenvalues in σ, the better the array
329 can detect (and help correct) errors of a prior estimate. *Le Hénaff et al.* (2009) show that a
330 useful choice of a discriminating spectral value is 1. In order to clarify this choice, let us
331 consider the *innovation vector d* and its second-order statistics:

332 $$d \equiv y^o - Hx^f \qquad (3)$$

333 $$\langle dd^T \rangle = R + HP^f H^T \qquad (4)$$

334 where y^o is the *observation vector* and x^f is the *forecast* (*prior*) *state vector*. Equation (4) is
335 the same as Eq. (1) in *Desroziers et al.* (2005). An intuitive criterion of array performance is
336 as follows:

337 1) If observational errors R dominate in Eq. (4), then most of the model-data discrepancies in
338 d are attributable to observational error, and observations are not being very useful at detecting
339 model uncertainties.

340 2) If prior state errors $HP^f H^T$ (the *representer matrix*) dominate, then most of the
341 discrepancies are attributable to model uncertainties, and observations can be expected to be
342 useful at identifying and correcting them.

343 Let us examine this criterion in array space. Using the orthogonality of array modes, it is easy
344 to show that the innovation covariance in Eq. (4) projected into array space, becomes:

345 $$E^i \equiv \mu^T R^{-\frac{1}{2}} < dd^T > R^{-\frac{1}{2}} \mu = I + \sigma, \qquad (5)$$

346 hence the choice of 1 as a discriminating spectral value. It follows:

347 *Criterion ArM1: Array performance is measured by the number of ranks k for which:*

348 $$1 \leq \sigma_k$$

349 Note that (1) this first criterion is only based on the space-time sampling scheme and on the
350 ensemble covariance; it does not require the actual values of observations; (2) it is not yet
351 expressed as an empirical consistency criterion for our ensemble. Now, when we have the
352 values of observations, Eq. (4) can be used to derive an empirical ensemble consistency
353 criterion. Innovation Eq. (3) can be formed, and $\langle dd^T \rangle$ can be calculated empirically and
354 compared to the right-hand side of Eq. (4). In effect, the innovation spread is the result of prior
355 uncertainties of both the model and observations; therefore, that spread should be statistically
356 consistent with the sum of prior model uncertainty estimates and observational uncertainty
357 estimates.

358 As above, this criterion is more advantageously examined in array space, i.e. in the form of Eq.
359 (5). Since $I + \sigma$ is diagonal, we focus on the diagonal of $E^i = diag\{e_k^i\}$, i.e. the innovation
360 variance in array space. Our second criterion writes:

361 > *Criterion ArMCA1: Empirical consistency is measured by the number of ranks k for which:*

362 $$1 - \tau \leq \frac{1 + \sigma_k}{e_k^i} \leq 1 + \tau$$

363 > *with τ the user-selected tolerance (e.g. $\tau = 0.1$ for 10% tolerance).*

364 In this study, we use the ArM1 and ArMCA1 criteria as implemented in the ArM tools library
365 *(De Mey-Frémaux, pers. comm.,* 2020*),* distributed as open source within the SDAP
366 assimilation platform (*De Mey-Frémaux, 2020:* https://sourceforge.net/projects/sequoia-dap/).
367 We check consistency in array space, also qualifying consistency results with their associated
368 multivariate patterns in observation space. In short, criterion ArM1 is an "array performance"
369 criterion based on how the observational array "observes" model uncertainties; criterion
370 ArMCA1 tests ensemble empirical consistency in terms of variances; other criteria are present
371 in the ArM tools but are not used here.

372 Our approach can be seen as an extension of the *Desroziers et al.* (2005) consistency diagnostic
373 on innovations (their Eq. (1)), which we project on the space of array modes.

374 We remove ensemble averages prior to analysis. In contrast to rank histogram analysis,
375 observations are perturbed, using a Gaussian random number to generate data distributions
376 with proper error estimates for each network (Table 2). Although the methodology allows for
377 nondiagonal *observational error covariance matrix*, we consider it to be diagonal in this study,
378 meaning that observational errors are considered statistically independent from each other. In
379 case of non-Gaussian distributions, an anamorphosis transformation is applied so as to
380 calculate array modes in the transformed space. For instance, in this study, model and data
381 chlorophyll samples are log-transformed prior to computing array modes.

382 ## 5 Results

383 ### 5.1 Rank histograms consistency analysis

384 In Figs. 3-5, we show Hovmöller plots of rank histograms as a means to analyse space-time
385 ensemble consistency. Under-dispersive rank histograms are characterized by a U-shape
386 diagram, since observations fall mostly in the outer ranks of the ensemble. In the context of a
387 Hovmöller plot of rank histograms, under-dispersion is illustrated by contrasting colours
388 between outer and central ranks (Fig. 3). In the same line of thinking, bias is depicted by having
389 large values only on one side of the histogram and flatness (i.e. $\delta \sim 1$) is verified for evenly
390 distributed pdf values at $\frac{1}{41} \sim 0.024$ across all ranks. Rank histograms for SST verify that EnsP
391 is generally under-dispersive and biased, though results vary depending on seasons and on the
392 use of different networks (Fig. 3). On the other hand, there are cases where observations are
393 evenly distributed within the ensemble spread despite persistent under-dispersion. The rank
394 histograms are in close agreement with the consistency analysis based on the OSTIA SST
395 innovation samples, presented in the companion article Part 1.

396 In order to illustrate dependency based on geographical region, we focus on three distinct areas
397 in the Bay of Biscay, namely the abyssal plain, the Armorican shelf and the English Channel
398 (Fig. 3). There is evidence of local error regimes where EnsP is either warm or cold biased
399 with respect to observations. From the latter we can link SST observational biases and
400 underestimated model errors potential to local dynamics. For instance, rank histogram flatness
401 is occasionally verified in the abyssal plain, whereas in the Armorican shelf and the English
402 Channel the ensemble is shifting from being warm biased in winter to cold biased in spring
403 with respect to observations. The results are associated with the spring shoaling of the
404 thermocline in the open ocean, as well as to coastal processes controlled by frontal activity of

405 freshwater river discharges over the Armorican shelf, and to tidal mixing in the English
406 Channel. There is also a marked difference between the two SST networks when used to
407 validate consistency against EnsP. The OSTIA SST fits better within the ensemble classes
408 during winter, whilst the consistency for the NWS SST is improved during spring. Overall, the
409 EnsP is notably under-dispersive and on average warm biased with respect to observations,
410 whilst cold biased in the English Channel.

411 Figure 4a shows a Hovmöller plot of rank histograms and Fig. 4b a map of ranks as a means to
412 analyse space-time ensemble consistency for sea-level. The SLA model equivalent is
413 calculated using a mean dynamic topography as in the companion article Part 1. The gridded
414 SLA product appears to be under-dispersive having a bias against the ensemble shifted between
415 seasons (Fig. 4a). This bias is most likely attributed to the seasonal steric cycle contributing to
416 sea-level variability being weak in the observations. As a consequence, rank histogram flatness
417 is not verified throughout the series.

418 Similar results are presented in the map of rank histograms for the along-track SLA product
419 (Fig. 4b). As in the companion article Part 1, we focus our analysis in late-winter for a few
420 consecutive days after having a model ensemble statistical spin-up for EnsP (Fig. 1d) and also
421 observing noticeable sea-level variability in the satellite observations. Strong biases are
422 apparent, both in the deeper areas of the domain and in the shelves. These biases also coincide
423 with the location of inconsistent tidal residual signals (both in the model and data) in the
424 English Channel. Contrasting colours in the Celtic Sea and near the shelf break hint at the
425 presence of high-frequency error processes currently unaccounted for in the model ensemble.
426 Under-dispersion and missing errors in the high-frequency band (e.g. open boundary
427 conditions in the shelves, which do not deal properly with high-frequency processes), is also
428 confirmed by the fact that there are only a few central ranks depicted in the map.

429 In Fig. 5, we present Hovmöller plots of rank histograms as a means to analyse ensemble
430 consistency with respect to different classes of chlorophyll. For this, we use the PFT dataset
431 against the model ensemble EnsPB which has the largest spread among the three ensembles
432 (Figs. 2b-d). Rank histograms for EnsPB verify that all ensembles are under-dispersive, with
433 EnsB being the least dispersive and EnsPB the most dispersive. The chlorophyll rank
434 histograms for EnsP (not shown) are comparable to those of EnsPB (Fig. 5), but with lower
435 levels of consistency. Rank histograms indicate a rather long statistical biogeochemical spin-
436 up period, on the order of 3 months (verified by rank histogram flatness for evenly distributed
437 pdf values), and persistent model underestimation of chlorophyll abundance. The spin-up
438 period corresponds only to the winter season characterised by low primary production. After
439 the spin-up period, the consistency is in general improved for total chlorophyll, as a result of
440 the onset of the nanophytoplankton spring bloom. On the other hand, diatoms appear to
441 degenerate the consistency of total chlorophyll. During successive spring blooms,
442 inconsistencies are seen in the peak, but better agreement in the onset and relaxation of the
443 blooms. This is explained by the fact that ocean colour peak values are of an order of magnitude
444 larger compared with model outputs, whilst PFT data fall within the ensemble spread during
445 the onset and relaxation phases of a bloom event. Overall, the most consistent configurations
446 are the nanophytoplankton in early-spring (i.e. primary bloom mainly in the abyssal plain) and
447 the diatoms in late-spring (i.e. secondary bloom mainly coastal and over the shelves).

448 **5.2   Array-space empirical consistency analysis**

449 In Fig. 6a, we show in a Hovmöller plot the variations in time of OSTIA SST array mode
450 spectra vs. modal rank (i.e. the rank of the array mode), including an EnsP consistency check
451 against OSTIA SST data. We used 39 array modes, corresponding to the 39 "degrees of
452 freedom" characterizing a 40-member de-biased ensemble. The ensemble spin-up period

10

453 appears as a period of low eigenvalues near the beginning of the time series, lasting from a few
454 days (in the head of the spectra) to a few weeks (in the tails). The array performance at
455 "detecting" model uncertainties, as per criterion ArM1, appears satisfactory from spin-up time
456 to the end of the series, with values above 1 across the spectra. Eigenvalues get larger in the
457 last two months, likely reflecting both the onset of a seasonal thermocline and upper-ocean
458 processes within the error subspace generated by our stochastic protocol (e.g. in response to
459 wind uncertainties). The loss of empirical consistency of EnsP with respect to OSTIA SST as
460 per criterion ArMCA1 appears as white "pixels". Consistency appears to be almost always
461 verified along the dominant array modes, mostly associated with large-scale patterns (as
462 illustrated in Fig.7). The number of ensemble inconsistency cases increases as one moves to
463 the tails of the spectra, mostly associated with smaller-scale and coastal patterns. Overall,
464 pattern consistency is fairly good with OSTIA SST.

465 Figure 6b shows the impact of subsampling the OSTIA data, mimicking the impact of using a
466 lower-resolution SST product for ensemble validation. However, although the general pattern
467 is similar, the statistical significance of the consistency analysis degrades significantly; only
468 ~50% of the array modes pass the ArM1 criterion (many more than with the product without
469 subsampling) and appear inconsistent in the ArMCA1 criterion. It is important to note that this
470 degradation is also felt for the dominant array modes, mostly associated with large-scale
471 patterns, except possibly near the end of the time series. Such a (random and systematic)
472 subsampling leads to a significant loss of information that could be used to constrain the high-
473 resolution model ensemble, if EnsP was to be used as an estimate of the model errors. Also,
474 high-resolution SST products appear necessary when it comes to validating eddy-resolving
475 ensembles, such as 1/36° here.

476 Is this degradation dependent upon the data product? The NWS SST observations are of higher
477 resolution compared with the OSTIA SST and therefore are able to "detect" a broader range of
478 model errors, including in the tail modes (not shown). A subsampling rate of one-sixth brings
479 up a resolution similar to the one-fifth subsampling of OSTIA dataset (~25 km). The
480 consistency analysis results were found to be comparable for both networks (Figs. 6b, c).

481 Let us now turn to data-space patterns of array modes, i.e. the eigenvectors over which our
482 empirical ensemble consistency analysis of EnsP is carried out. Figure 7 shows examples of
483 such patterns for both one-fifth subsampled OSTIA (7a-c) and one-sixth NWS (7d), along with
484 the result of the ArMCA1 criterion for each mode. We focus on May 31, 2012 which is
485 characterized by a slightly higher energy in the spectra compared with neighbouring periods
486 (Figs. 6b-c). Unlike rank histograms depicted in Fig. 3, the OSTIA and NWS array modes are
487 very similar (as illustrated in Figs.7a, d for mode 1), because the subsampled observational
488 schemes are similar, but consistency analysis results do not have to be. Not surprisingly for a
489 regularly-spaced dataset, the first array mode patterns (Fig.7a, d) resembles the structure of the
490 SST spread (Fig. 1b).

491 For the datasets at hand, the dominant patterns appear to be mostly typical of large-scale and
492 mesoscale processes (Figs.7a, b); seeing zero amplitudes in low-order modes for the English
493 Channel indicates that the array will not be able to correct the SST statistically dominant model
494 errors. The spatial scales appear to decrease as one moves to the tail of the spectrum, and the
495 coastal features become more pronounced (as illustrated in Fig.7c); simultaneously, the
496 ensemble consistency is verified less frequently.

497 When an ensemble is found to be inconsistent with observations along a particular direction
498 (here, an array mode), a plausible reason is that other error processes must be active in the
499 model in addition to the ones which are at work across the ensemble. This can be verified by
500 checking for model underdispersion. However, as is the case in the examples above,

11

501 insufficient resolution of the observations can also lead to statistical inconsistency, impacting
502 mostly small scales and coastal scales.

503 In Fig. 8a, we show a Hovmöller plot of variations in time of the gridded SLA array mode
504 spectra, including an EnsP consistency check against gridded SLA data. Again, we used 39
505 array modes. The dataset is relatively coarse at ~25 km resolution and therefore is not
506 subsampled. As before, spectral values smaller than one (light grey in Fig.8a) are associated
507 with poor array performance at "detecting" model uncertainties as per the ArM1 criterion, and
508 white areas depict inconsistent array modes as per ArMCA1 criterion. On average, on the order
509 of 20 array modes sit above the observational noise floor. However, only a fraction of those
510 modes, on the order of 10 on average, show pattern consistency as per ArMCA1 criterion.
511 Overall, consistency of EnsP with respect to the gridded SLA product is not as good as it was
512 with respect to the SST product.

513 Let us turn to the patterns of eigenvectors in an effort to explain the weak consistency. In Figs.
514 8b-e, we show examples of consistent and inconsistent patterns of gridded SLA array modes
515 on April 30, 2012. Consistency is verified for the first two array modes shown (ranks 1 and 5),
516 featuring large-scale sea-level gradients over the whole domain including the shallow Celtic
517 Sea and the Eastern Biscay shelf (Fig. 8b-c). Both higher array modes (ranks 10 and 20) shown
518 in Figs. 8d-e are inconsistent – they seem to be dominated by mesoscale and submesoscale sea-
519 level signals (or at least, their 0.25° representation) as well as regional-scale sea-level signals
520 over the shelves and in the English Channel. Small-scale inconsistent higher array modes in
521 the abyssal plain can be explained by the mesoscale low-frequency decorrelation between
522 members, generating phase differences between mesoscale features. From these results we can
523 infer that assimilating the 0.25° gridded product in EnsP would probably lead to unsatisfactory
524 results at the mesoscale and in coastal areas, since error vicinities in the model ensemble and
525 in observations seem at least partly inconsistent with each other in that scale range. Of course,
526 one can introduce representativity errors in the observational error covariance matrix to make
527 things consistent again, but small scales are expected to be inadequately controlled by
528 assimilation.

529 We now check the consistency of EnsP against the along-track sea-level data. We focus on the
530 same period and on the same tracks as in the rank histograms analysis with the same dataset,
531 starting on February 25, 2012, for 10 consecutive days. The analysis is performed considering
532 together all tracks that would be assimilated in a 10-day assimilation cycle. Therefore, each
533 array mode, characteristic of the 10-day multi-track network, spans both space and time. Figure
534 9a shows the array mode spectrum over the 10-day period. As per criterion ArM1, almost all
535 eigenvalues are larger than the observational noise threshold (except a few tail modes) and as
536 per criterion ArMCA1 most of them are consistent. This is significantly improved compared
537 to the consistency of EnsP with respect to the gridded sea-level product.

538 In order to get a bit further into which patterns and underlying processes appear to be
539 (in)consistent, we examine the corresponding eigenvectors. Figures 9b-c show the first two
540 ranks of array modes for the multi-track network; Figs. 9d-e are the same for the higher array
541 modes with ranks 19 and 20 respectively. Both Figs. 9b and 9c show large-scale sea-level
542 gradients, encompassing open-ocean and shelf regions. The patterns in Fig. 9b are generally of
543 a bipolar nature with near zero amplitudes along the continental shelf break for most of the
544 tracks in the region, hinting at shelf/open-ocean exchange processes at work in the model's
545 error subspace. In Figs. 9d-e, we show two examples of higher array modes, with ranks 19 and
546 20 being consistent and inconsistent, respectively. Higher array modes show a wide range of
547 spatial scales, including large-scale over the shelves and tracks characteristic of mesoscale
548 signals in the open-ocean, with gradients more pronounced than in the gridded product. In most

12

549 cases, the higher array modes are consistent and because it is above observational noise (as
550 shown in Fig. 9a) their consistency is meaningful. We therefore have evidence that along-track
551 SLA data could, if assimilated using EnsP for covariances, bring useful consistent information
552 at large scales and at the mesoscale.

553 Central to this work is the consistency of biogeochemical model ensembles against our PFT
554 product as derived from satellite ocean colour measurements. In Fig. 10, we show Hovmöller
555 plots of variations in time of univariate PFT array mode spectra, including EnsP, EnsB and
556 EnsPB consistency analysis against PFT data, using again 39 array modes. Calculations were
557 performed in log array space (i.e. involving log transformation from data space prior to array
558 mode calculations), without subsampling data. The array mode spectra in Fig.10 exhibit strong
559 variations in time, with several peaks corresponding to differential blooms across ensembles
560 for the various chlorophyll classes during the onset and relaxation of those events. We note
561 however that this is a gridded product with gaps, so part of those variations are also explained
562 by the spatial data coverage variations with time (Fig. 10a; superimposed black line). This does
563 not question our statistical approach, since poor data coverage will logically lead to poorer
564 array performance at detecting ensemble variance; but that dependency must be kept in mind
565 when interpreting the results in terms of processes.

566 With the ensemble strategy we adopted, one can examine the array performance and the
567 consistency individually for physical (EnsP) and biogeochemical (EnsB) uncertainties, and for
568 both (EnsPB) together, all in the same PFT data space; in that manner, we can see the individual
569 and combined effects of both components (Fig. 10). As already noted in Part 1 article, it appears
570 that physical perturbations (EnsP) have greater impact on biogeochemical model errors than
571 biogeochemical sources and sinks perturbations. The higher EnsP ensemble variance for PFT
572 variables explains also the shorter statistical spin-up period on the order of 1 month, whereas
573 EnsB shows a spin-up period on the order of 3 months, shown as overly inconsistent (i.e. the
574 first three months in Figs. 10a-c vs. 10d-f). It also appears that visually "adding" the
575 nanophytoplankton and diatoms spectra does not come close to describing the total chlorophyll
576 spectra, in particular for EnsP and EnsPB (Figs. 10a-c and 10g-i), whilst being partially verified
577 for EnsB (Figs. 10d-f). The spectra derived from diatoms in EnsP and EnsPB appears not to
578 contribute to the total chlorophyll spectra, the latter having eigenvalues similar to those of
579 nanophytoplankton.

580 We see three possible classes of explanations to this result: (1) it is likely that the constant
581 observational error of 0.3 mg/m^3 over the whole domain and for all classes, is unrealistic,
582 particularly for diatoms exhibiting higher local uncertainties in the shelves and coastal regions;
583 (2) it is possible that our decomposition of total chlorophyll into two size classes (or four binned
584 into two as discussed in Section 3.3) is not entirely relevant process-wise (i.e. combining one
585 PFT with characteristic silicate limitation with one without), effectively leading to a statistical
586 ill-posed issue; (3) total chlorophyll as resulting from a variety of processes (especially when
587 physical perturbations are applied) will have higher statistical complexity (higher number of
588 "degrees of freedom") than either nanophytoplankton or diatoms taken independently, leading
589 to "purple" spectra with more tail modes not represented on Figs. 10a and 10g, while Figs. 10c
590 and 10i show "redder" diatoms spectra.

591 Figure 11 shows examples of low and high gridded PFT array modes and consistency status of
592 EnsP and EnsB vs. the PFT dataset (EnsPB eigenvectors are similar to EnsP; not shown). Let
593 us focus on March 28, 2012, where for this specific date the PFT are gap-free over the Bay of
594 Biscay facilitating our analysis at all scales. As for rank histogram analyses, we choose to
595 investigate the period during early spring, because consistency can be easily explained by the
596 onset of the chlorophyll abundance primary bloom (Fig. 2). In effect, for a positive oriented

13

597 variable such as chlorophyll, bloom-related model spread increases when abundance increases
598 during a bloom event, therefore chances for pattern consistency are higher. We note that this is
599 a very different result compared to rank histograms which show degraded consistency during
600 blooms. This is because rank histograms are sensitive to model-data biases amplified during
601 blooms (in contrast to array modes free from biases). The latter is also supported by the fact
602 that the biogeochemical model ensembles are under-dispersive, due to model underestimation
603 of chlorophyll abundance.

604 The PFT first array modes using EnsP and EnsB show consistent patterns and are compatible
605 in structure with the model's second-order statistical moments respectively (Figs. 11a, f vs.
606 Figs. 2b, c). Another remark is that the first array modes using EnsP and EnsB are different
607 (Figs. 11a-c vs. Figs. 11d-f). When physics is perturbed (i.e. EnsP) the total chlorophyll
608 eigenvectors appear as large-scale open ocean patterns controlled by nanophytoplankton
609 primary production (Figs. 11a-b). When biogeochemical source and sink terms are perturbed
610 (i.e. EnsB) we observe mesoscale patterns for all classes, with nanophytoplankton again
611 defining the eigenvectors of total chlorophyll (Figs. 11d-e). For both ensembles, diatom
612 measurements appear to detect model errors mostly on the shelves, but their contribution for
613 the first array mode for total chlorophyll is limited (Figs. 11c, f).

614 For the higher modes we observe several combinations of consistent and inconsistent modes
615 across phytoplankton types and total chlorophyll. In general, when both phytoplankton types
616 are found to be consistent (inconsistent), then total chlorophyll is also likely to be found
617 consistent (inconsistent). Mixed consistency results between chlorophyll classes are also
618 observed (less frequently), but the non-mixed examples are the most informative to investigate
619 (Figs. 11g-l). When physics is perturbed the PFT array mode 25 is able to detect model errors
620 for both chlorophyll classes at small-scale (Figs. 11g-i). Surprisingly, for the higher array
621 modes using EnsP the diatoms appear to contribute to the spatial variability of total chlorophyll
622 at small-scale, especially in the shelves (Figs. 11g-i). By contrast, when biogeochemical source
623 and sink terms are perturbed the model-based PFT array mode 25 appears not to be consistent
624 with PFT data at the mesoscale (Figs. 11j-l). The fact that EnsB generates chiefly eigenvectors
625 with mesoscale patterns, implies that having identical ocean physics across all members limits
626 the potential of the PFT measurements to detect biogeochemical model errors at small-scale
627 (as shown for example for EnsP in Figs. 11g-i).

628 **6   Discussion and conclusions**

629 This study is Part 2 of a two-part series following a companion article Part 1 aimed at
630 generating ocean model ensembles. Part 2 article focuses on: (1) sophisticated ensemble
631 model-data comparison methods, one of them published here for the first time based on a new
632 criterion in the space of array modes, and (2) applying those methods for the first time with
633 phytoplankton functional type data derived from ocean colour.

634 The empirical consistency analysis focused on satellite observations (SST, SLA and ocean
635 colour), in concert with model ensembles of ocean physics and biogeochemistry. We used a
636 high-resolution configuration for the Bay of Biscay, as a means to investigate the model error
637 subspace generated by our stochastic protocol in a companion article Part 1, both in the open
638 and coastal ocean. In order to better understand the couplings between physics and
639 biogeochemistry we examined three model ensemble experiments: perturbing only physics,
640 perturbing only biogeochemical source and sink terms, and perturbing both simultaneously.
641 Below, we synthesize results from the two consistency methods in an attempt to assess the
642 reliability of model ensembles with respect to observations.

14

643 Rank histograms for physical properties showed a large dependency based on geographical
644 region and on season for both SST and SLA networks. In most cases, rank histograms showed
645 large biases between model and data, and were limited because of model ensemble underspread
646 and because of weak variability in the observations. In addition, there were high-frequency
647 errors in the observations that were not present in the model ensemble. Rank histograms for
648 the ocean colour PFT showed persistent model underestimation and underspread for
649 chlorophyll abundance, with some improvement for nanophytoplankton after a spin-up period
650 on the order of 3 months during the winter low primary productivity. Rank histograms have
651 been used successfully as a reliability tool identifying on several occasions consistent model-
652 data configurations and attributing this result to physical and biogeochemical processes, such
653 as the spring shoaling of the thermocline, the frontal activity in the shelves explained by river
654 plume migration, the tidal mixing in the English Channel (*Karagiorgos et al.*, 2020), and to a
655 lesser extent the chlorophyll abundance during spring, mainly on the onset and relaxation of
656 bloom events.

657 Array modes were performed using innovation samples in array space and therefore, model-
658 data distributions were free from biases hindering empirical consistency of error patterns (as
659 in some cases for the rank histograms). A typical result using array modes in the context of
660 stochastic modelling is that insufficient resolution of the verifying observations can lead to
661 statistical inconsistency, impacting mostly small and coastal scales. High-resolution datasets
662 (and model ensembles) can improve array modes consistency at small-scale, as long as the
663 following assumptions are valid: (a) data errors are uncorrelated, (b) data errors are small in
664 comparison to model-data misfit and (c) the model ensembles are not under-dispersive. When
665 ensembles are found to be inconsistent with observations along an array mode, a plausible
666 reason is that other error processes must be active in the model, in addition to the ones at work
667 across the ensemble. For instance, model errors in physical processes currently unaccounted
668 for are attributable to residual tidal errors (due to local tidal fronts and occasional Kelvin waves
669 propagating along the coasts), to the non-isostatic response of atmospheric pressure, and to
670 high-frequency errors in open boundaries over the shelves (*Vervatis et al.*, 2021). In addition,
671 complex processes in the biogeochemical model are simplified by making use of only a few
672 model parameters. Biogeochemical parameterizations controlling the growth rate and grazing
673 of phytoplankton classes in the model are based on approximations and therefore, stochastic
674 modelling of these parameters may improve model performance (*Garnier et al.*, 2015).

675 Array modes for both SST networks (i.e. OSTIA and NWS) showed that despite their
676 differences in production and resolution, if subsampled, can provide comparable information
677 to detect model errors, from shortly after the ensemble spin-up to the end of the series (in
678 contrast to rank histograms). Their consistency was verified for the large-scale and open ocean,
679 but also for the small-scale and coastal SST patterns. Array modes pattern consistency between
680 the model ensemble perturbing physics and the sea-level datasets was in general verified at
681 large-scale. The gridded SLA product showed unsatisfactory results at the mesoscale and in
682 coastal areas, whereas the along-track sea-level showed that, if assimilated, can bring
683 potentially useful information at the mesoscale.

684 The most important findings for the array modes using PFT against ocean biogeochemical
685 ensembles can be summarised as follows. A large ensemble variance can lead to an improved
686 PFT array performance, considering biogeochemical model uncertainties stemming mainly
687 from stochastic physics. Consistency results can be further enhanced if we consider a two-way
688 coupling and a feedback from the bio-optical model (due to changes in chlorophyll, leading to
689 increased model spread) to the physical model for the solar radiation penetration in the water
690 column. We performed a few simulations (not shown) but we decided not to activate the two-
691 way coupling, because the onset and relaxation of the spring bloom may occur earlier and more

15

692   rapidly in the model compared with observations in the region (*Gutknecht et al.*, 2019).
693   Additive spectra of nanophytoplankton and diatoms cannot describe total chlorophyll spectra.
694   One plausible explanation is that EnsP and EnsB state vectors (i.e. their anomalies from the
695   ensemble mean) are not statistically independent (perhaps as an artefact of the limited ensemble
696   size). This is proven also by the fact that ensemble variance for EnsPB sometimes can be
697   unexpectedly small, as if physics and biogeochemistry processes compensated, cf. companion
698   article Part 1. Consequently, there is no reason for array mode eigenspectra to be additive on a
699   rank-by-rank basis nor hierarchised in the same way (in contrast to other spectra, e.g. Fourier
700   and Wavelet Transform). Another point is that there is no reason our ensembles should be
701   orthogonal, because they are not built this way. The array mode spectra give an idea of the
702   number of "degrees of freedom" of the ensembles in data space, and of the very high temporal
703   variability of that number. For instance, the bloom periods are characterized by larger numbers
704   of "degrees of freedom", apparently peaking at 39 (40 minus mean). Other plausible
705   explanations may be the unrealistic observational error set globally at $0.3 \ mg/m^3$ for all PFT
706   and also, the total chlorophyll decomposition of four PFT binned into two not being entirely
707   relevant process-wise.

708   In general, the data PFT errors are not negligible and are related to the size-class (*Brewin et*
709   *al*., 2017; *Laiolo et al*., 2021). Errors are lower for the small size classes and higher for the
710   large size classes (with dinoflagellates having the higher errors of all PFT), and increased with
711   increasing chlorophyll. This is owing to the nature of how the satellite PFT error is computed.
712   Chlorophyll *a* uncertainties (e.g. root mean square error and bias) for each PFT are assigned
713   based on optical water type membership at a given satellite pixel (*Brewin et al.*, 2017). It is
714   expected that observational errors are cross-correlated, both across functional types and
715   spatially for each PFT. In fact, each PFT is computed as a function of the same total chlorophyll
716   product, and the same procedure is adopted to compute the errors of the different PFT (*Brewin*
717   *et al.*, 2017). The total chlorophyll product itself is expected to have spatially correlated errors.
718   This is due to both atmospheric effects (e.g. cloud cover) and in-water sources of errors, in
719   particular in the coastal zone, due to the coloured dissolved organic matter (CDOM) inputs that
720   degrade ocean colour near the coast (e.g. terrestrial CDOM in river plumes). This is also
721   confirmed by the PFT spatial error gradients and the gradients of the concentrations
722   themselves, being stronger for diatoms than nanophytoplankton in the coastal zone (*Brewin et*
723   *al*., 2017; *Ciavatta et al*., 2018). Cross-correlations are expected to be lower in the open ocean
724   and deeper areas. The representation of such uncertainty and correlated errors has been so far
725   neglected in ocean colour data assimilation (*IOCCG*, 2020). In our application, if we used such
726   PFT uncertainties and data correlations, the array modes consistency would have been
727   degraded, pertaining to the fact that ocean colour datasets are provided in high-resolution (and
728   therefore, spatial data correlations may not be negligible).

729   Pattern-selective consistency analysis showed that low-rank eigenvectors appear as large-scale
730   and mesoscale, mainly controlled by nanophytoplankton in the open ocean; diatom
731   measurements appear to detect model errors mostly on the shelves. For the higher modes,
732   biogeochemical model errors appear to be detected at small-scale only when physics is
733   perturbed. By contrast, when only biogeochemical source and sink terms are perturbed, the
734   model-based high-rank modes appear not to be consistent with PFT data at the mesoscale,
735   limiting also the potential to detect model errors at small-scale due to identical physical
736   processes across all members.

737   We recommend using methods adapting and estimating the **R** and **Q** *observational* and *model*
738   error covariance matrices, respectively. The ArM methodology can provide pattern- and scale-
739   dependent ensemble consistency checks, facilitating the qualification of ensembles to provide
740   useful error covariance estimates in regional systems for ulterior coastal downscaling.

741 The next step of this study will be dedicated to the investigation of ensemble consistency based
742 on array modes: (1) performing multivariate analysis between physics and biogeochemistry
743 (e.g. SST vs. total chlorophyll), and between phytoplankton size classes, using information for
744 the spatial distribution of observational errors; and (2) taking into account correlated
745 observational errors. To that end, an additional criterion will be introduced to check the
746 diagonality of the innovation covariance matrix in the space of array modes.

761 **References**

762 Anderson, J., 1996. A method for producing and evaluating probabilistic forecasts from
763   Ensemble model integrations, J. Climate, 9, 1518–1530.

764 Andersson, E., 2003. Modelling of innovation statistics. Proceedings of the Workshop on
765   recent developments in data assimilation for atmosphere and oceans. ECMWF, Reading,
766   UK, 153-164.

767 Anderson, J.L., 2009. Spatially and temporally varying adaptive covariance inflation for
768   ensemble filters. Tellus A, 61: 72-83. doi:10.1111/j.1600-0870.2008.00361.x.

769 Auclair, F., P. Marsaleix, and P. de Mey-Frémaux, 2003. Space-time structure and dynamics
770   of the forecast error in a coastal circulation model of the Gulf of Lions. Dynamics of
771   Atmospheres and Oceans, Elsevier, 36 (4), pp.309-346. 10.1016/S0377-0265(02)00068-4.

772 Aumont, O., Ethé, C., Tagliabue, A., Bopp, L., and Gehlen, M., 2015. PISCES-v2: an ocean
773   biogeochemical model for carbon and ecosystem studies. Geosci. Model Dev. 8, 2465-2513.

774 Brewin, R. J. W., Ciavatta S., Sathyendranath S., Jackson T., Tilstone G., Curran K., Airs R.
775   L., Cummings D., Brotas V., Organelli E., Dall' Olmo G., and Raitsos D. E., 2017.
776   Uncertainty in Ocean-Colour Estimates of Chlorophyll for Phytoplankton Groups. Front.
777   Mar. Sci. 4:104. doi: 10.3389/fmars.2017.00104.

778 Brewin, R. J. W., S. Sathyendranath, T. Hirata, S. J. Lavender, R. Barciela, and N. J. Hardman-
779   Mountford, 2010. A three-component model of phytoplankton size class for the Atlantic
780   Ocean, Ecol. Modell., 221, 1472–1483, doi: 10.1016/j.ecolmodel.2010.02.014.

781 Brewin, R. J. W., Sathyendranath, S., Jackson, T., Barlow, R., Brotas, V., Airs, R., et al., 2015.
782   Influence of light in the mixed layer on the parameters of a three-component model of
783   phytoplankton size structure. Remote Sens. Environ. 168, 437–450. doi:
784   10.1016/j.rse.2015.07.004.

785 Candille, G., and Talagrand, O., 2005. Evaluation of probabilistic prediction systems for a
786   scalar variable. Q. J. R. Meteorol. Soc., 131, 2131-2150.

787 Candille, G., Brankart, J.-M., and Brasseur, P., 2015. Assessment of an ensemble system that
788   assimilates Jason-1/Envisat altimeter data in a probabilistic model of the North Atlantic
789   ocean circulation. Ocean Science 11, 425–438.

790 Charria, G., Lamouroux, J., and De Mey, P., 2016. Optimizing observational networks
791   combining gliders, moored buoys and FerryBox in the Bay of Biscay and English Channel.
792   Journal of Marine Systems, 162, 112-125, http://dx.doi.org/10.1016/j.jmarsys. 2016.04.003.

793 Chelton, D. B., Schlax, M. G., Samelson, R. M., 2011. Global observations of nonlinear
794   mesoscale eddies, Prog. Oceanogr., 91, 167–216, doi:10.1016/j.pocean.2011.01.002.

795 Ciavatta, S., Brewin, R. J. W., Skákala, J., Polimene, L., de Mora, L., Artioli, Y., and Allen, J.
796   I., 2018. Assimilation of Ocean-Colour Plankton Functional Types to Improve Marine
797   Ecosystem Simulations. Journal of Geophysical Research: Oceans, 123(2), 834–854,
798   https://doi.org/10.1002/2017JC013490.

799 Ciavatta, S., Kay, S., Brewin, R. J. W., Cox, R., Di Cicco, A., Nencioli, F., and Tsapakis, M.,
800   2019. Ecoregions in the Mediterranean Sea Through the Reanalysis of Phytoplankton
801   Functional Types and Carbon Fluxes. Journal of Geophysical Research: Oceans, 124(10),
802   6737–6759, https://doi.org/10.1029/2019JC015128.

803 Desroziers, G., Berre, L., Chapnik, B., Poli, P., 2005. Diagnosis of observation, background
804   and analysis-error statistics in observation space. Q. J. R. Meteorol. Soc. 131, 3385–3396.
805   https://doi.org/10.1256/qj.05.108.

806 Donlon, C.J., Martin, M., Stark, J., Roberts-Jones, J., Fiedler, E., and Wimmer, W., 2012. The
807   Operational Sea Surface Temperature and Sea Ice Analysis (OSTIA) system. Remote
808   Sensing of the Environment, doi: 10.1016/j.rse.2010.10.017 2011.

809 Evensen, G., 2003. The Ensemble Kalman Filter: theoretical formulation and practical
810   implementation. Ocean Dyn. 53, 343-367.

811 Ford, D., 2019. Assessing the role and consistency of satellite observation products in global
812   physical-biogeochemical ocean reanalysis. Ocean Sci. Discuss. 1–25.
813   https://doi.org/10.5194/os-2019-118.

814 Garnier, F., Brankart, J.M., Brasseur, P., and Cosme, E., 2016. Stochastic parameterizations of
815   biogeochemical uncertainties in a 1/4° NEMO/PISCES model for probabilistic comparisons
816   with ocean color data. Journal of Marine Systems, 155, 59–72.

817 Ghantous, M., Ayoub, N., De Mey-Frémaux, P., Vervatis, V., and Marsaleix, P., 2020.
818   Ensemble downscaling of a regional ocean model. Ocean Modell., 145,
819   https://doi.org/10.1016/j.ocemod.2019.101511.

820 Gharamti, M. E., J. Tjiputra, I. Bethke, A. Samuelsen, I. Skjelvan, M. Bentsen, and L. Bertino,
821   2017. Ensemble data assimilation for ocean biogeochemical state and parameter estimation
822   at different sites, Ocean Modelling, 112, 65-89,
823   https://doi.org/10.1016/j.ocemod.2017.02.006.

824 Gutknecht, E., Reffray, G., Mignot, A., Dabrowski, T., and Sotillo, M. G., 2019. Modelling the
825   marine ecosystem of Iberia–Biscay–Ireland (IBI) European waters for CMEMS operational
826   applications, Ocean Sci., 15, 1489–1516, https://doi.org/10.5194/os-15-1489-2019.

18

827 Hamill, T.M., 2001. Interpretation of Rank Histograms for Verifying Ensemble Forecasts.
828   Mon. Wea. Rev., 129, 550-560, https://doi.org/10.1175/1520-0493(2001)129<0550:
829   IORHFV>2.0.CO;2.

830 Ide, K., Courtier P., Ghil M., and Lorenc A., 1997. Unified notations for data assimilation:
831   operational, sequential and variational. J. Met. Soc. Japan, 75(1B):181-189.

832 IOCCG, 2020. Synergy between Ocean Colour and Biogeochemical/Ecosystem Models.
833   Dutkiewicz, S. (ed.), IOCCG Report Series, No. 19, International Ocean Colour
834   Coordinating Group, Dartmouth, Canada.

835 Janjić, T., Bormann N., Bocquet M., Carton J.A., Cohn S.E., Dance S.L., Losa S.N., Nichols
836   N.K., Potthast R., Waller J.A., Weston P, 2018. On the representation error in data
837   assimilation, Q J R Meteorol Soc.,144,1257–1278.

838 Karagiorgos, J., V. Vervatis, and S. Sofianos, 2020. The Impact of Tides on the Bay of Biscay
839   Dynamics. J. Mar. Sci. Eng., 8, 617.

840 Kourafalou V.H., P. De Mey, M. Le Hénaff, G. Charria, C.A. Edwards, R. He, M. Herzfeld,
841   A. Pasqual, E.V. Stanev, J. Tintoré, N. Usui, A.J. Van Der Westhuysen, J. Wilkin and Zhu,
842   X., 2015a. Coastal Ocean Forecasting: system integration and validation. Journal of
843   Operational Oceanography, http://dx.doi.org/10.1080/1755876X.2015.1022336.

844 Kourafalou, V.H., P. De Mey, J. Staneva, N. Ayoub, A. Barth, Y. Chao, M. Cirano, J. Fiechter,
845   M. Herzfeld, A. Kurapov, A.M. Moore, P. Oddo, J. Pullen, A.J. van der Westhuysen and
846   Weisberg, R.H., 2015b. Coastal Ocean Forecasting: science foundation and user benefits.
847   Journal of Operational Oceanography, http://dx.doi.org/10.1080/ 1755876X.2015.1022348.

848 Lamouroux, J., G. Charria, P. De Mey, S. Raynaud, C. Heyraud, P. Craneguy, F. Dumas and
849   Le Hénaff, M., 2016. Objective assessment of the contribution of the RECOPESCA network
850   to the monitoring of 3D coastal ocean variables in the Bay of Biscay and the English
851   Channel. Ocean Dynamics, 66(4), 567-588, http://dx.doi.org/10.1007/s10236-016-0938-y.

852 Le Hénaff, M., P. De Mey and Marsaleix, P., 2009. Assessment of observational networks with
853   the Representer Matrix Spectra method – Application to a 3-D coastal model of the Bay of
854   Biscay. Ocean Dynamics, 59, 3-20, DOI 10.1007/s10236-008-0144-7.

855 Leonardo, L., R. Matear, M. Soja-Woźniak, D. J. Suggett, D. J. Hughes, M. E. Baird, M. A.
856   Doblin, 2021. Modelling the impact of phytoplankton cell size and abundance on inherent
857   optical properties (IOPs) and a remotely sensed chlorophyll-a product, Journal of Marine
858   Systems, 213, 103460, https://doi.org/10.1016/j.jmarsys.2020.103460.

859 Madec, G., 2012. Nemo ocean engine, Tech. rep., NEMO team.

860 Mattern, J.P., Edwards, C.A., and Moore, A.M., 2018. Improving Variational Data
861   Assimilation through Background and Observation Error Adjustments. Mon. Wea. Rev.,
862   146, 485–501, https://doi.org/10.1175/MWR-D-17-0263.1.

863 Oke, P. R., and P. Sakov, 2008. Representation Error of Oceanic Observations for Data
864   Assimilation. J. Atmos. Oceanic Technol., 25, 1004–1017,
865   https://doi.org/10.1175/2007JTECHO558.1.

866 Pujol, M.-I., Faugère, Y., Taburet, G., Dupuy, S., Pelloquin, C., Ablain, M., and Picot, N.,
867   2016. DUACS DT2014: the new multi-mission altimeter data set reprocessed over 20 years,
868   Ocean Sci., 12, 1067-1090, doi:10.5194/os-12-1067-2016.

869 Quattrocchi, G., P. De Mey, N. Ayoub, V. Vervatis, C.-E. Testut, G. Reffray, J. Chanut and Y.
870   Drillet, 2014. Characterisation of errors of a regional model of the Bay of Biscay in response

871   to wind uncertainties: a first step toward a data assimilation system suitable for coastal sea
872   domains. Journal of Operational Oceanography, Volume 7, Number 2, August 2014, pp. 25-
873   34(10).

874   Sakov, P., G. Evensen and L. Bertino, 2010. Asynchronous data assimilation with the EnKF.
875   Tellus A. 62(1): 24-29, http://dx.doi.org/10.1111/j.1600-0870.2009.00417.x.

876   Sieburth, John McN. Smetacek, Victor Lenz, Jürgen, 1978. Pelagic ecosystem structure:
877   Heterotrophic compartments of the plankton and their relationship to plankton size
878   fractions, Limnology and Oceanography, 23, doi: 10.4319/lo.1978.23.6.1256.

879   Simon, E., and Bertino, L., 2009. Application of the Gaussian anamorphosis to assimilation in
880   a 3-D coupled physical-ecosystem model of the North Atlantic with the EnKF: a twin
881   experiment. Ocean Sci. 5, 495-510.

882   Skakala, J., Ford, D., Brewin, R. J. W., Mc Ewan, R., Kay, S., Taylor, B., de Mora, L., and
883   Ciavatta, S., 2018. The assimilation of phytoplankton functional types for operational
884   forecasting in the North-West European Shelf. Journal of Geophysical research - Oceans,
885   123 (8), 5230-5247, doi: 10.1029/2018JC014153.

886   Song, H., Edwards, C.A., Moore, A.M., Fiechter, J., 2016. Data assimilation in a coupled
887   physical-biogeochemical model of the California current system using an incremental
888   lognormal 4-dimensional variational approach: Part 3—Assimilation in a realistic context
889   using   satellite   and   in   situ   observations.   Ocean   Model.   106,   159–172.
890   https://doi.org/10.1016/j.ocemod.2016.06.005.

891   Vervatis, V. D., C.E. Testut, P. De Mey, N. Ayoub, J. Chanut, and G. Quattrocchi, 2016. Data
892   assimilative twin-experiment in a high-resolution Bay of Biscay configuration: 4D EnOI
893   based on stochastic modelling of the wind forcing. Ocean Modelling, 100, 1-19,
894   http://dx.doi.org/10.1016/j.ocemod.2016.01.003.

895   Vervatis, V. D., De Mey-Frémaux, P., Ayoub, N., Karagiorgos, J., Ghantous, M., Kailas, M.,
896   Testut, C.-E., and Sofianos, S., 2021. Assessment of a regional physical-biogeochemical
897   stochastic ocean model. Part 1: ensemble generation, Ocean modell., under review.

20

898 **Table 1.** Stochastic model ensembles (cf. companion article Part 1 by *Vervatis et al*., 2021).

Ensemble	SPPT/SPP-AR(1)		
EnsP	Physics	Atm. forcing	U_{air}, T_{air}, SLP
		Parameters	c_d, c_e, c_h, c_b
EnsB	Biogeochemistry	sources-minus-sinks of 24 prognostic variables $SMS(C)$	
EnsPB	Physics & Biogeochemistry	EnsP & EnsB	

899 abbreviations: SPPT - stochastic perturbed parameterized tendencies; SPP - stochastic
900 perturbed parameters; AR(1) - first-order autoregressive processes; U_{air} - wind velocities; T_{air}
901 - air temperature; SLP - sea level pressure; c_d, c_e, c_h - wind drag and turbulent coefficients; c_b
902 - bottom drag; $SMS(C)$ - sources minus sinks of biogeochemical tracers C.

903 **Table 2.** Observational networks.

CMEMS Product Identifiers (http://marine.copernicus.eu/)*		Error
OSTIA SST L4 gridded 0.05^o	SST_GLO_SST_L4_NRT_OBS_010_001	
NWS SST L4 gridded 0.04^o	SST_ATL_SST_L4_REP_OBS_010_026	$0.5\ ^oC$
SLA L3 along-track $14\ km$	SEALEVEL_GLO_PHY_L3_REP_OBS_008_062	
SLA L4 gridded 0.25^o	SEALEVEL_GLO_PHY_L4_REP_OBS_008_047	$0.05\ m$
Chlorophyll a gridded 0.05^o	Phytoplankton Functional Types - PFT (*Brewin et al*., 2017)	$0.3\ mg/m^3$

904 *All datasets are provided at daily frequency.

21
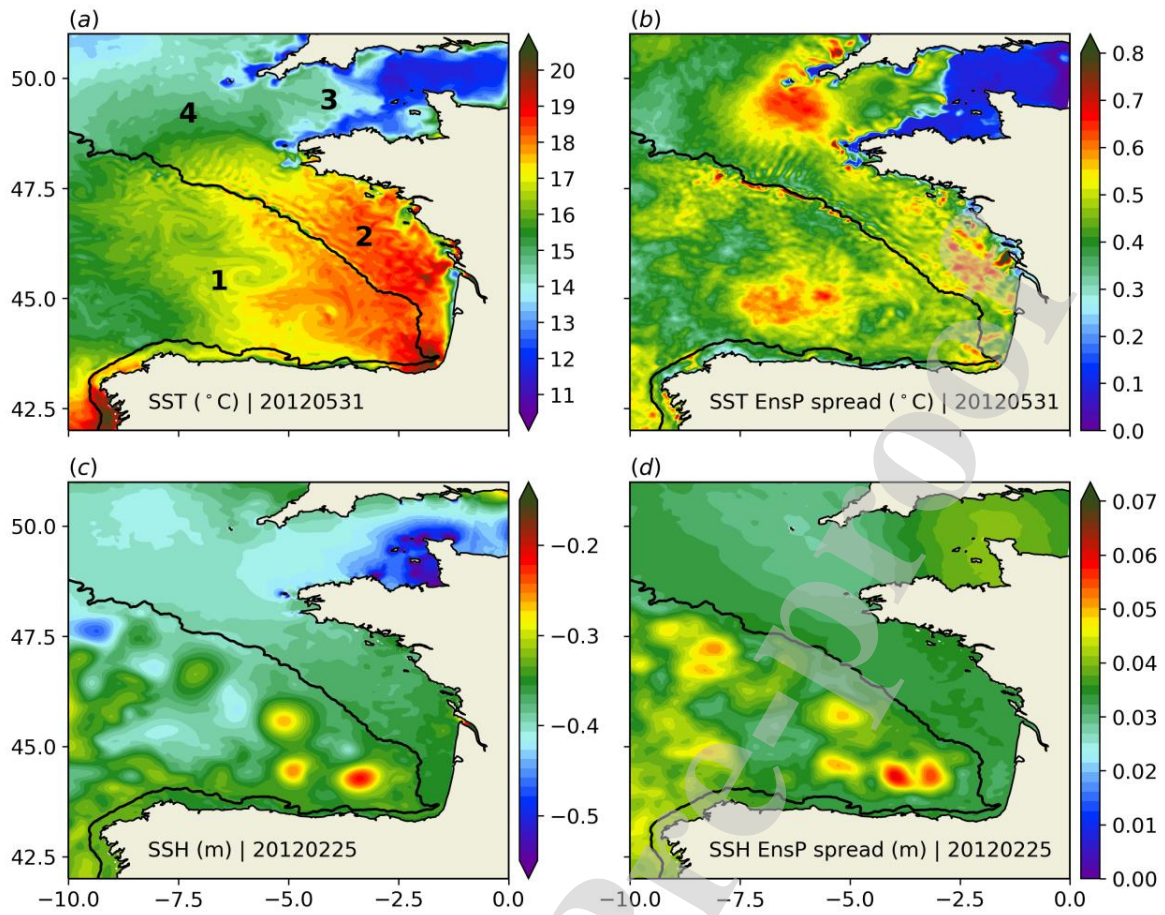
Figure 1   (a-b) Deterministic run SST and model ensemble EnsP spread ($°C$) on May 31, 2012. (c-d) Same for SSH (m) on February 25, 2012. Fig. 1a depicts the characteristic areas in the Bay of Biscay discussed in the text: 1-abyssal plain, 2-Armorican shelf, 3-English Channel, 4-Celtic shelf. Black line denotes the 200 m isobaths.
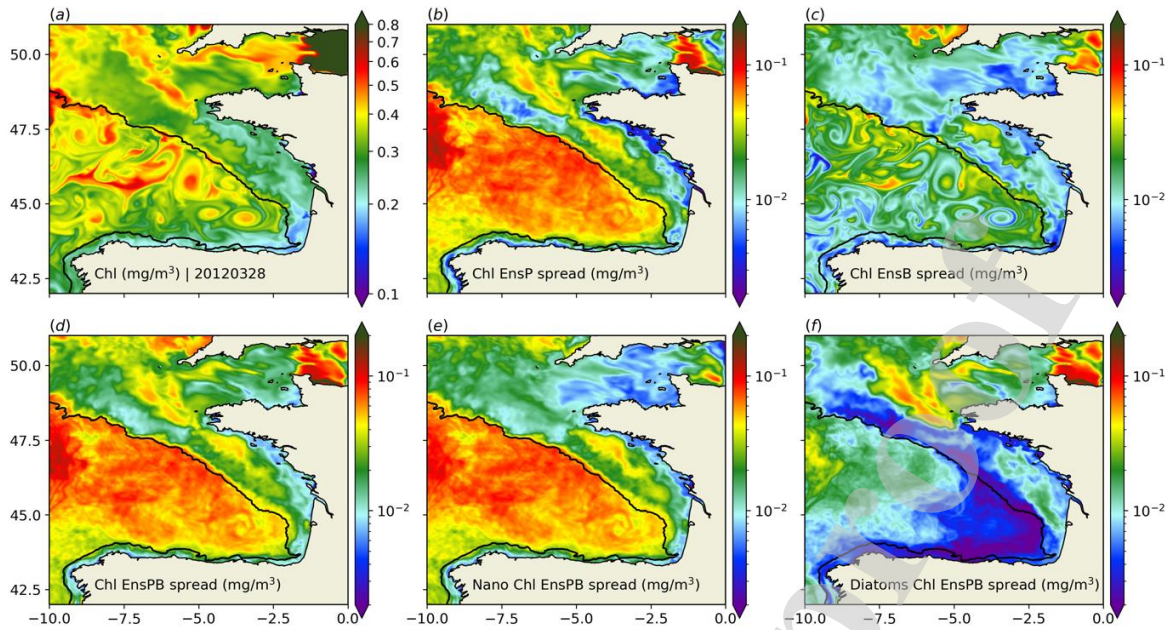
Figure 2 (a-d) Total chlorophyll deterministic run and model ensembles spreads EnsP, EnsB, EnsPB (mg/m^3) on March 28, 2012. (e-f) Same with (d) model ensemble spread EnsPB for nanophytoplankton and diatoms chlorophyll (mg/m^3) respectively.

23

914
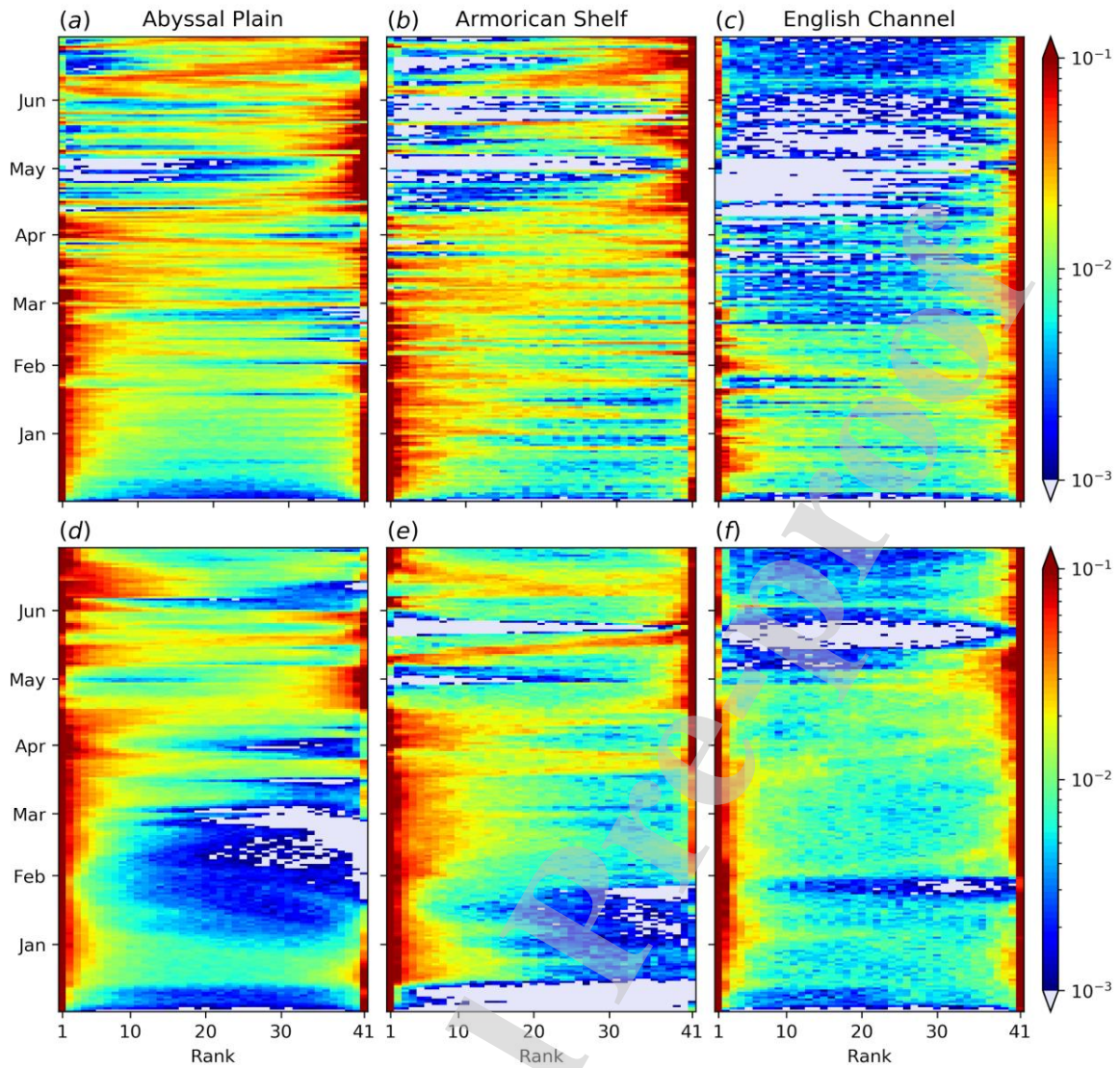
Figure 3 Hovmöller plot of rank histograms (x-axis: rank, y-axis: time, colorbar: pdf) between ensemble EnsP and SST L4 datasets: (a-c) OSTIA, (d-f) NWS. Regional consistency is checked for the (left to right): abyssal plain, Armorican shelf and English Channel. Rank histogram flatness is verified for pdf values at $\frac{1}{41} \sim 0.024$ (green-yellow in colorbar).

24

919
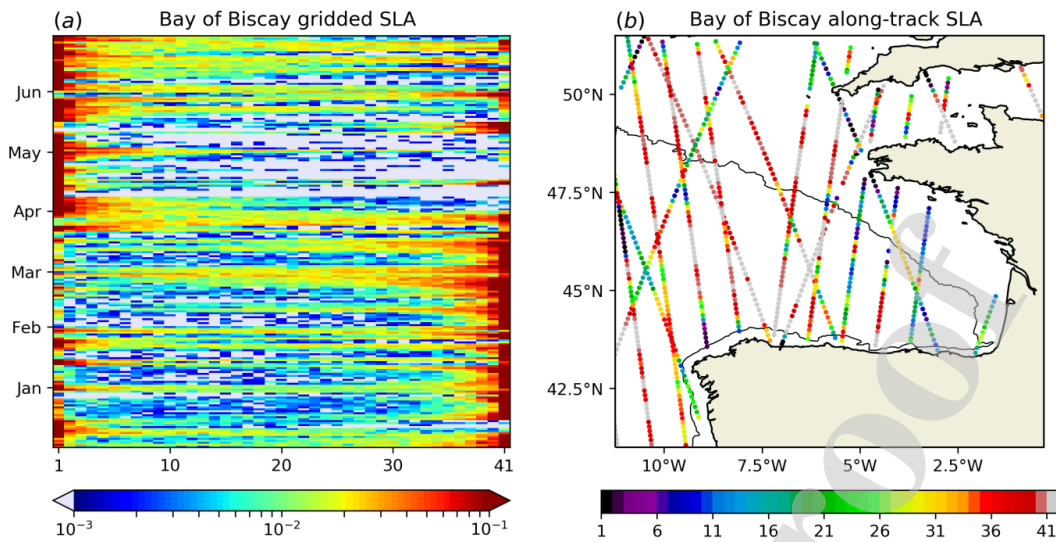
Figure 4 (a) Hovmöller plot of rank histograms (x-axis: rank, y-axis: time, colorbar: pdf) between ensemble EnsP and SLA L4 gridded dataset for the Bay of Biscay, and (b) map of ranks for along-track SLA L3 dataset with respect to the ensemble EnsP (colorbar: rank), starting on February 25, 2012, and for 10 consecutive days, including ascending and descending tracks in the domain.
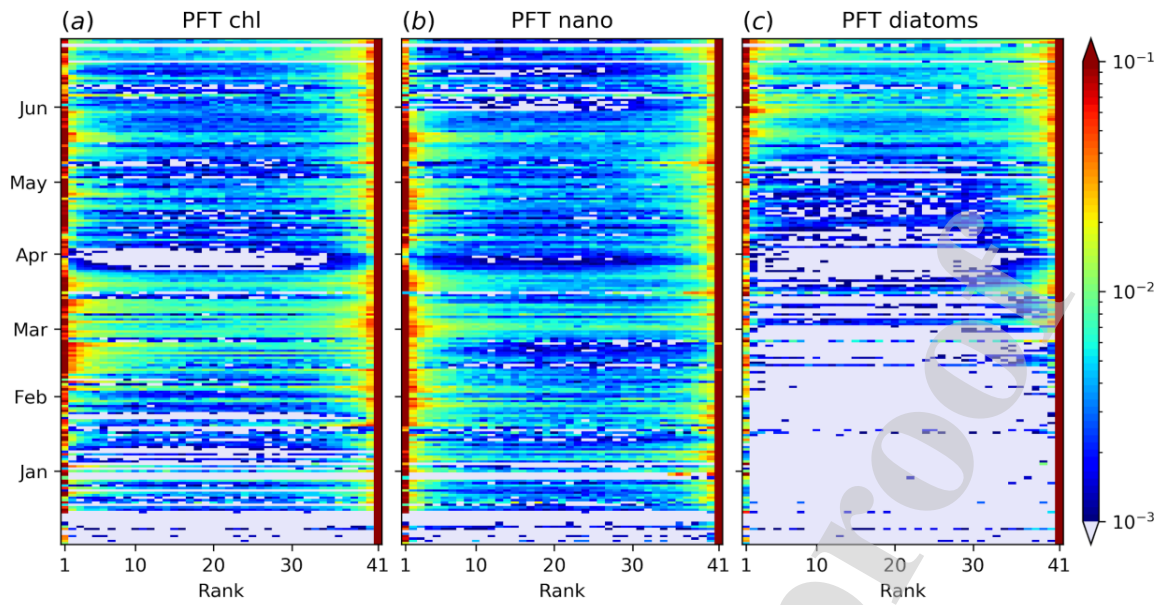
Figure 5   Hovmöller plot of rank histograms (x-axis: rank, y-axis: time, colorbar: pdf) between ensemble EnsPB and PFT dataset: (a) total chlorophyll, (b) nanophytoplankton and (c) diatoms chlorophyll.

26

929
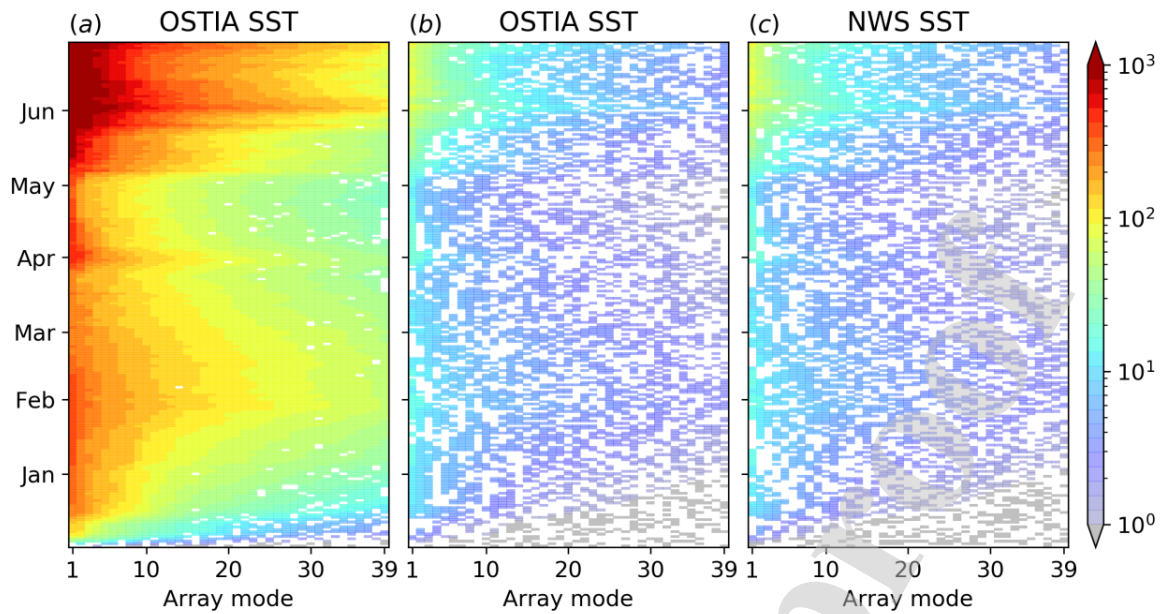
Figure 6 Hovmöller plot of variations in time of SST array mode spectra vs. modal rank (i.e. the rank of the array mode), including an EnsP consistency check against (a-b) OSTIA and (c) NWS SST data. Colorbar: array mode spectra as of criterion ArM1; eigenvalues smaller than one (the observational noise floor in array space; grey pixels) denote error modes marginally detectable by the array. White pixels depict inconsistent array modes as per criterion ArMCA1 (the higher modes are also mostly inconsistent as per criterion ArM1). (a) No data subsampling, (b) one-fifth subsampling rate (i.e. one data point every fifth OSTIA point retained), and (c) one-sixth subsampling rate.

27
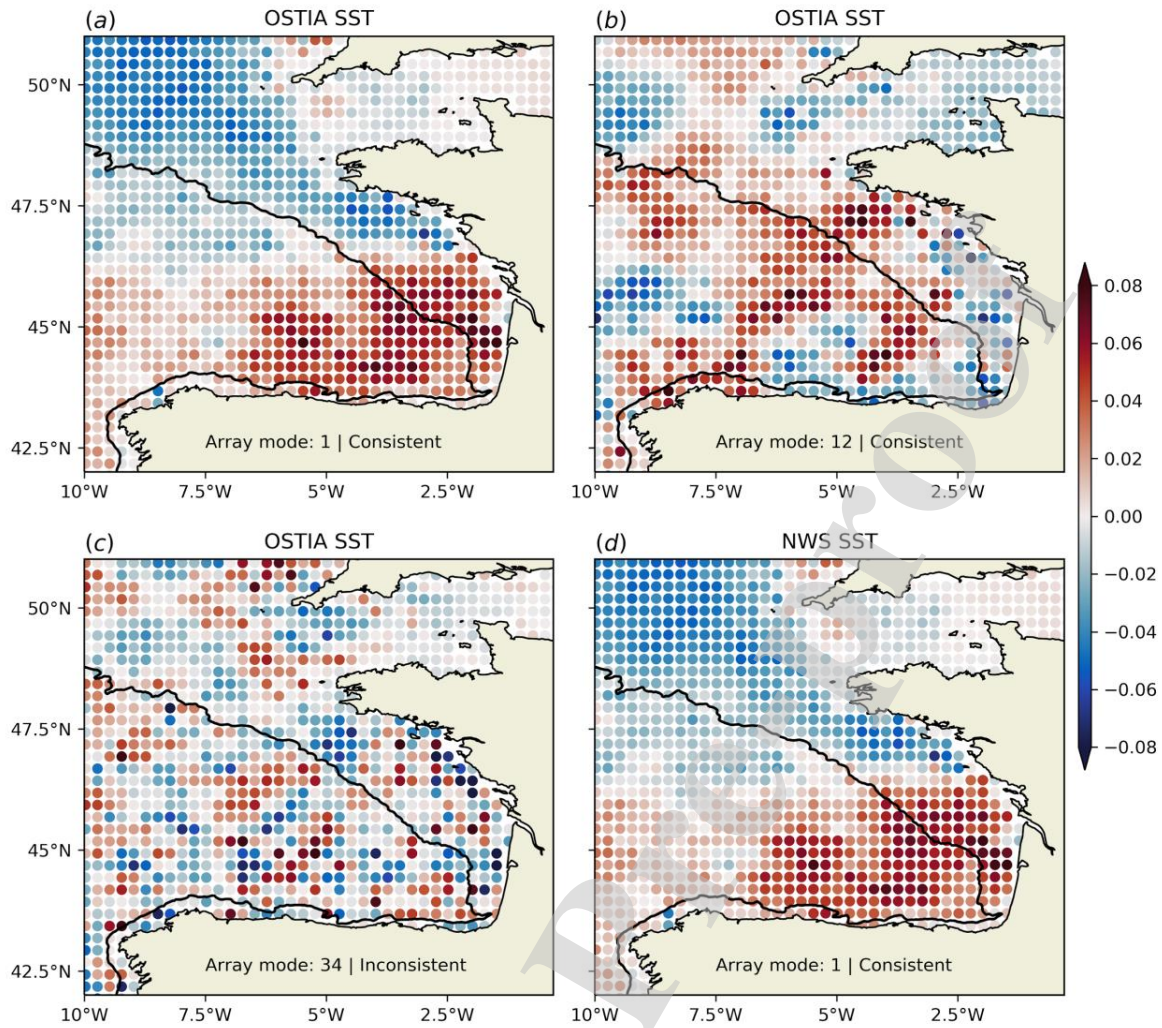
Figure 7 (a-c) Array modes 1, 12 and 34 for EnsP as "seen" from OSTIA SST on May 31, 2012, using one-fifth subsampling rate, and (below as text) corresponding results of the ArMCA1 consistency criterion using OSTIA SST observations; the 1st and 12th array modes are consistent; array mode 34 is inconsistent. (d) Same as (a) for NWS SST and one-sixth subsampling rate. Colorbar: array mode amplitude (no units) on (subsampled) data grid.
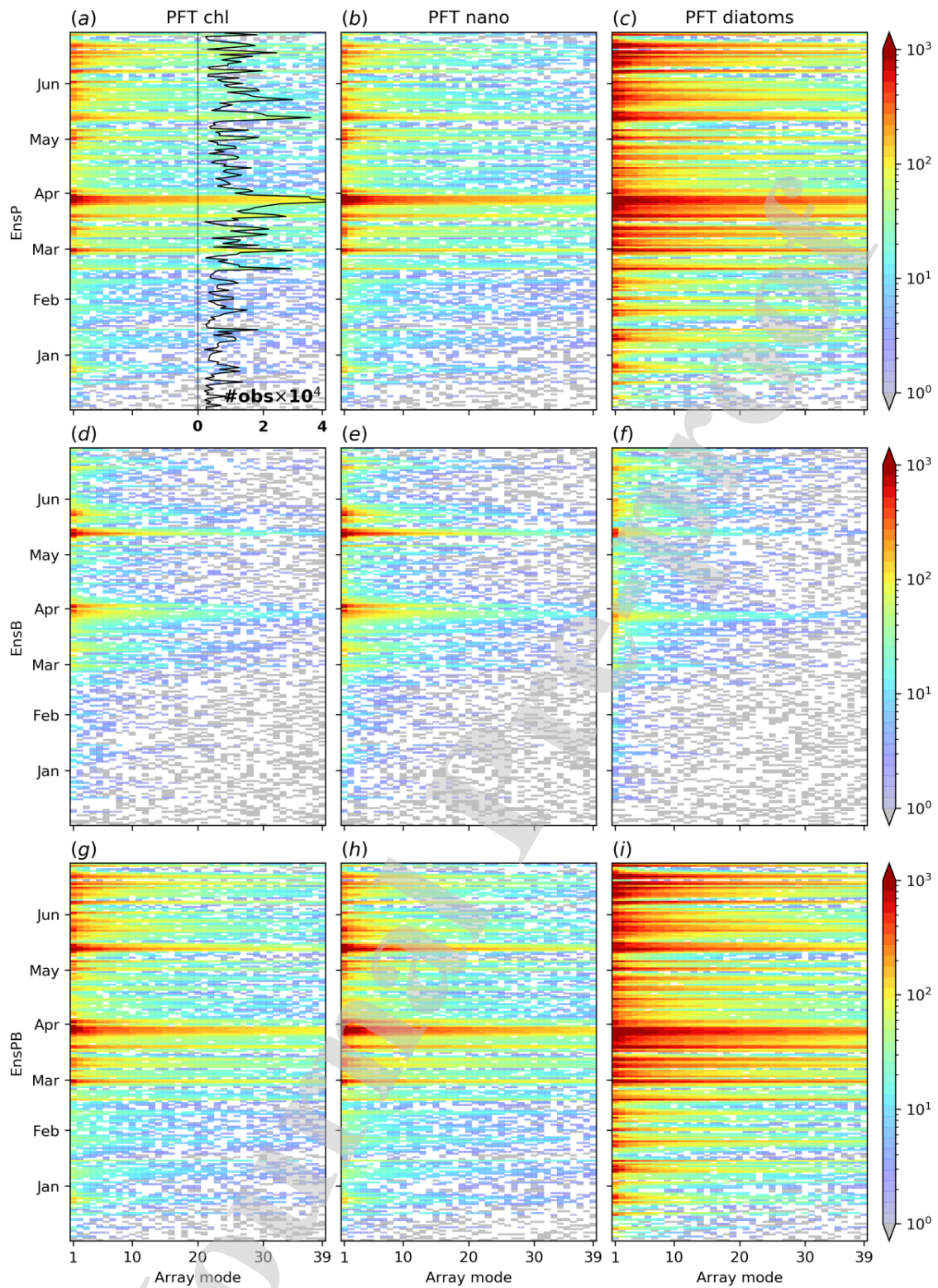
28

944
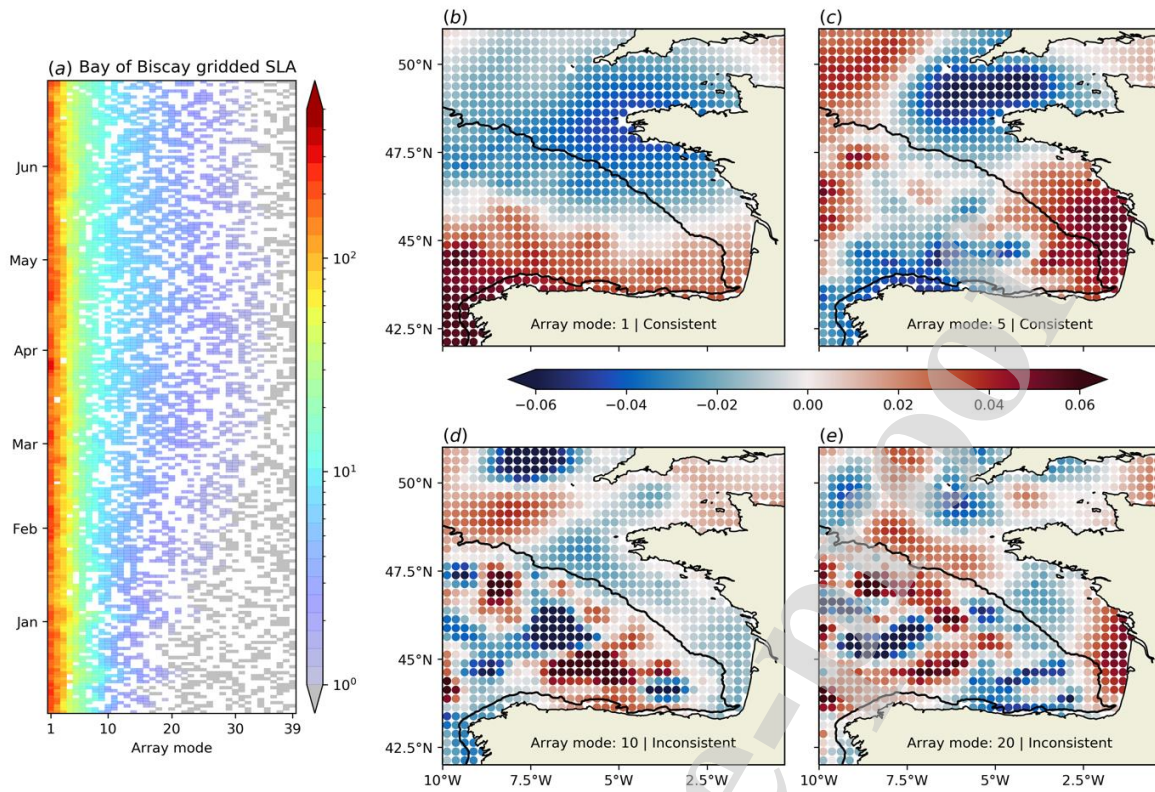
Figure 8   (a) Hovmöller plot of variations in time of gridded SLA array mode spectra vs.
modal rank, including an EnsP consistency check against gridded SLA data. (b-e) Examples of
consistent and inconsistent gridded SLA array modes on April 30, 2012 for EnsP. Colorbars
and units as in Figs. 6 and 7.
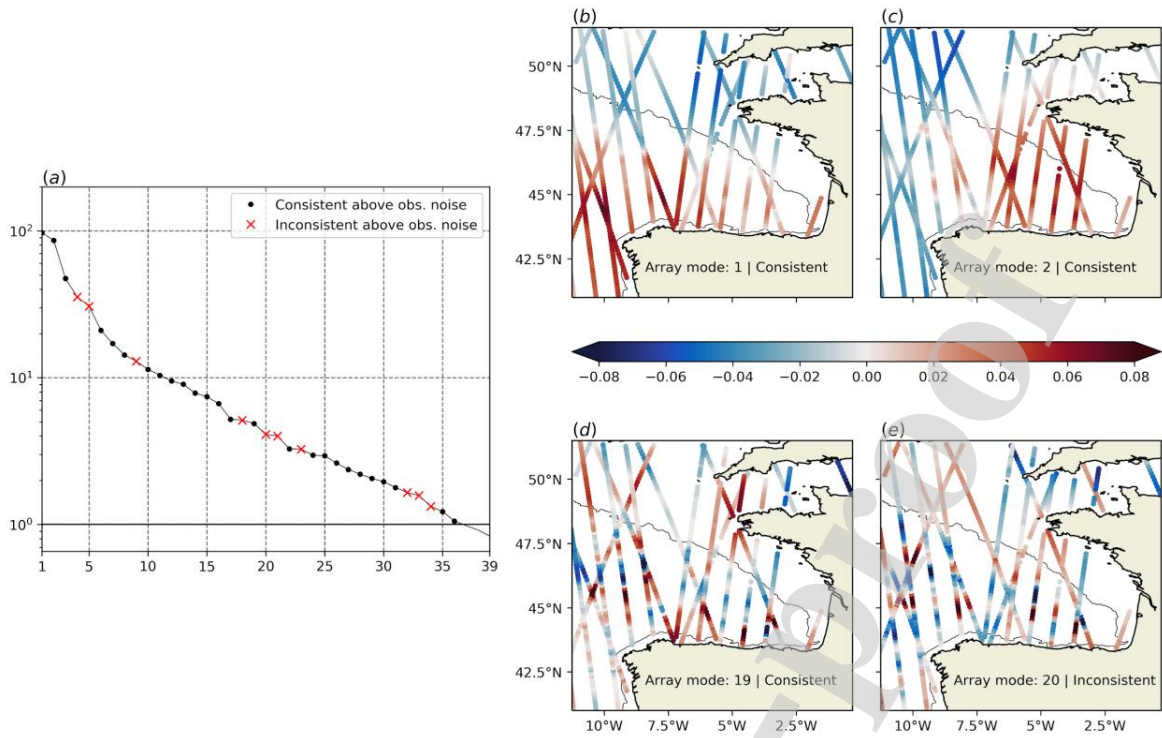
Figure 9 (a) Along-track SLA L3 array mode spectrum for the same period as in Fig. 4b, considering all tracks that would be assimilated in a 10-day assimilation cycle. Black and red markers for eigenvalues above the observational noise floor (= 1 in array space) denote consistent and inconsistent modes respectively. (b-c) Multi-track network consistent array modes of ranks 1 and 2 respectively (no units; all times "flattened", i.e. 2D representation of array modes including time space); (d-e) same as (b-c) for a higher consistent array mode of rank 19 and for an inconsistent array mode of rank 20 respectively. Colorbar and units as in Figs. 6 and 7.

Figure 10 (a-c) Hovmöller plots of variations in time of PFT array mode spectra vs. modal rank, including EnsP consistency checks against PFT data for total chlorophyll, nanophytoplankton, and diatoms respectively as shown; (d-f) same as (a-c) for EnsB; (g-i) same as (a-c) for EnsPB. Chlorophyll distributions have been log transformed. Colorbars and units as in Fig. 6. Fig. 10a superimposed black line: number of data with largest values corresponding to full data coverage of the domain i.e. #obs $\sim(4 \cdot 10^4)$.

958

959
960
961
962
963
964

31
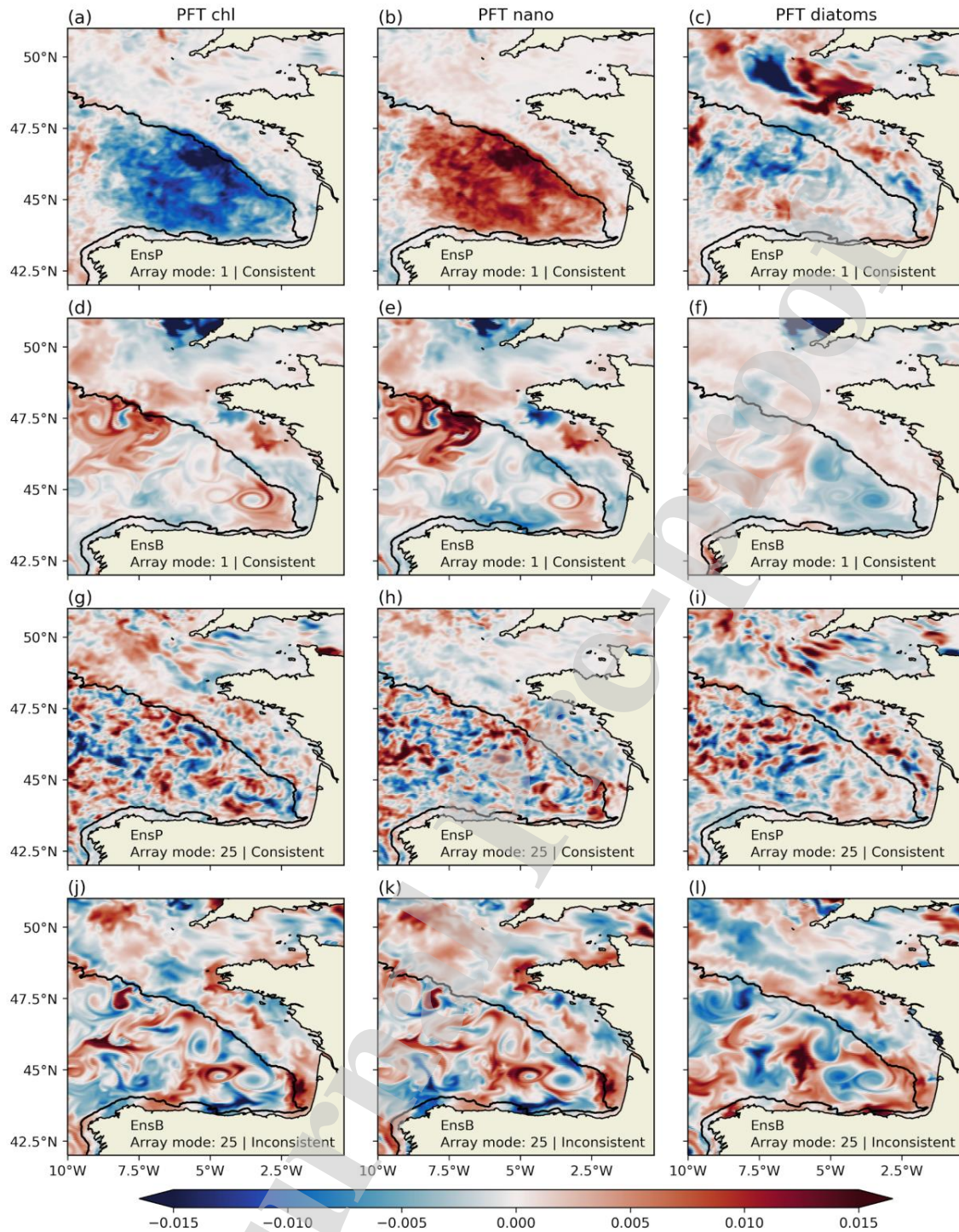
Figure 11   Examples of array modes for EnsP and EnsB on March 28, 2012, as "seen" from PFT data points, and (below as text) corresponding results of the ArMCA1 consistency criterion using PFT data: (a-c) array modes at rank 1 using EnsP (all consistent); (d-f) array modes at rank 1 using EnsB (all consistent, but different); (g-i) array modes at rank 25 using EnsP (all consistent); (j-l) array modes at rank 25 using EnsB (all inconsistent). PFT gridded data (gappy in general) have no gaps on that particular date in the Bay of Biscay. (left column) Total chlorophyll; (center) nanophytoplankton; (right column) diatoms. No data subsampling. Array modes calculated in log array space. Colorbar and units as in Fig. 7.

32

Highlights

- Model-data biases and model underspread revealed in rank histograms
- Consistent SST array modes at large scales and at small-scale
- Along-track array modes showed useful consistent information at the mesoscale
- Consistent PFT array modes at small-scale perturbing physics
- Additional error processes active in the model for inconsistent configurations

Authors' contribution statement using CRediT

1) Vassilios D. Vervatis: conceptualization, methodology, software, visualization, formal analysis, investigation, writing – original draft, writing – review and editing.
2) Pierre De Mey-Frémaux: conceptualization, methodology, software, formal analysis, writing – original draft, writing – review and editing.
3) Nadia Ayoub: conceptualization, formal analysis, writing – original draft, writing – review and editing.
4) John Karagiorgos: software, visualization, formal analysis.
5) Stefano Ciavatta: data curation, writing – review and editing.
6) Robert J. W. Brewin: data curation, writing – review and editing.
7) Sarantis Sofianos: conceptualization, resources.

The corresponding author,

Vassilios Vervatis

Declaration of interests

☒ The authors declare that they have no known competing financial interests or personal relationships that could have appeared to influence the work reported in this paper.

☐The authors declare the following financial interests/personal relationships which may be considered as potential competing interests:

Supplementary material

Fig. S1 presents the temporal variability of the PFT data in the Bay of Biscay, during the period December, 2011 to June, 2012. We also show the ocean colour L4 total chlorophyll product used in the Part 1 article (*Vervatis et al.*, 2021) and we verify that concentrations are of the same order to those of the PFT total chlorophyll. According to this, we categorised the four satellite PFT (pico, nano, diatoms and dino) into the two broad size groups in PISCES (nano or diatoms), in a manner most representative, ensuring that the total biomass (chlorophyll) from the model and satellite data can be compared like-for-like.

PFT diatoms and nanophytoplankton contribute together approximately more than 80% in total chlorophyll, whereas picoplankton contributes at about 10% and dinoflagellates less than 10% (Fig. S1). PFT diatom chlorophyll concentration is an order of magnitude larger compared with dinoflagellates and nanophytoplankton is about three times larger than picoplankton chlorophyll concentration (Fig. S1). In Fig. S2, we show the spatial distribution of the four satellite PFT and the total chlorophyll during the peak of the spring bloom on March 28, 2012. We confirm that the satellite micro class (i.e. diatoms and dino) is driven primarily by diatoms, far more abundant in the satellite data, with the two functional types being highly correlated in spatial. Fig. S3 presents scatter plots of combined vs. non-combined PFT chlorophyll, verifying the close relationship between functional types in a size class-based approach.

We also present results from one-on-one comparisons between model and PFT data, as opposed to the size class-based categorization merging different functional types. Figure S4 shows Hovmöller plot of rank histograms between EnsPB and PFT, in the same way as Figs. 5b-c, with one main difference: in Figs. S4a-b we do not combine the nano functional type with pico, nor we combine diatoms with dino. Rank histogram results for the nano class are degraded when pico and nano PFT data are not combined together in late-winter and early-spring when a primary bloom occurs (Fig. 5b vs. Fig. S4a). The latter may suggest that PISCES nano can be representative of a broader phytoplankton community, accounting also for smaller size classes. Rank histogram results are almost identical throughout the whole period for the micro class, regardless of whether dino and diatoms are combined together or not (Fig. 5c vs. Fig. S4b). Model-data one-on-one array mode consistency results (not shown) are in practice indistinguishable by visual inspection with the results presented in Figs. 10 and 11, confirming the validity of the size class-based approach.
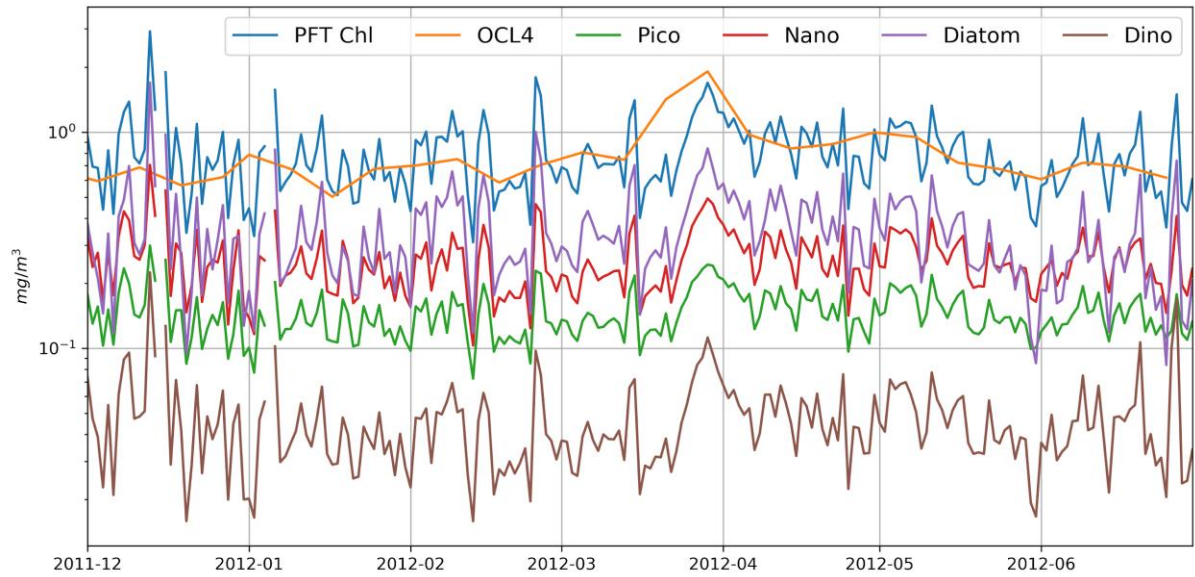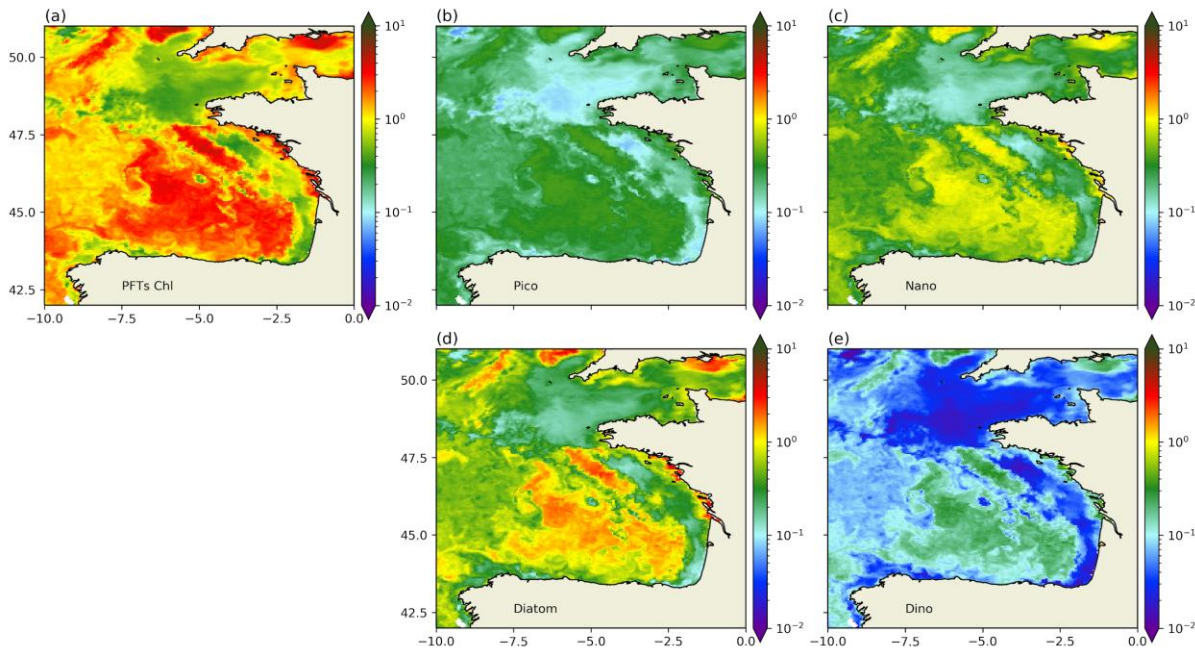
1005

1006 **Figure S1** Ocean colour L4 (8-day frequency) and PFT (daily) chlorophyll concentration
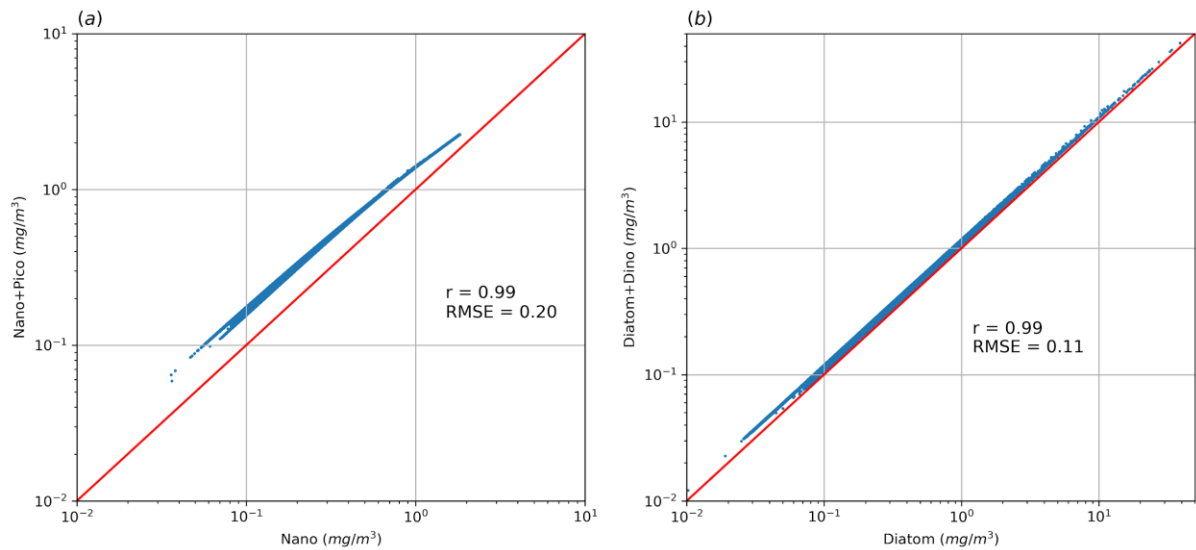1007 (mg/m^3) in the Bay of Biscay from December, 2011 to June, 2012.


1008

1009 **Figure S2** Spatial distribution of (a) PFT total chlorophyll and (b) pico, (c) nano, (d)
1010 diatoms, (e) dino concentrations (mg/m^3) on March 28, 2012.

34

1011

1012 **Figure S3** Scatter plots of chlorophyll concentrations in mg/m^3 on March 28, 2012: (a)
1013 PFT (nano and pico) vs. only nano, (b) PFT (diatoms and dino) vs. only diatoms. r is the
1014 correlation coefficient, RMSE the root mean square error (mg/m^3) and with red the 1:1 line.
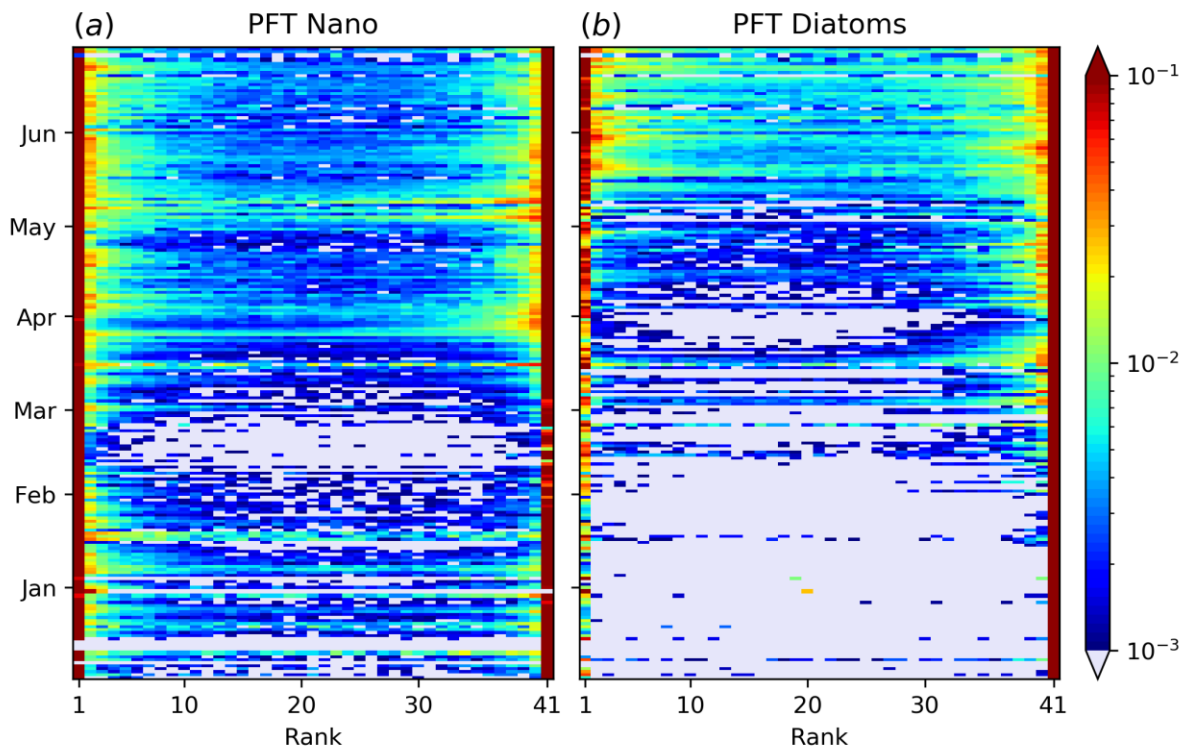
1015

1016 **Figure S4** Hovmöller plot of rank histograms (same as in Figs. 5b-c) between EnsPB and
1017 PFT (a) nano not combined with pico, and (b) diatoms not combined with dino.